

# Chapter 3

## Mie theory

### 3.1 Introduction

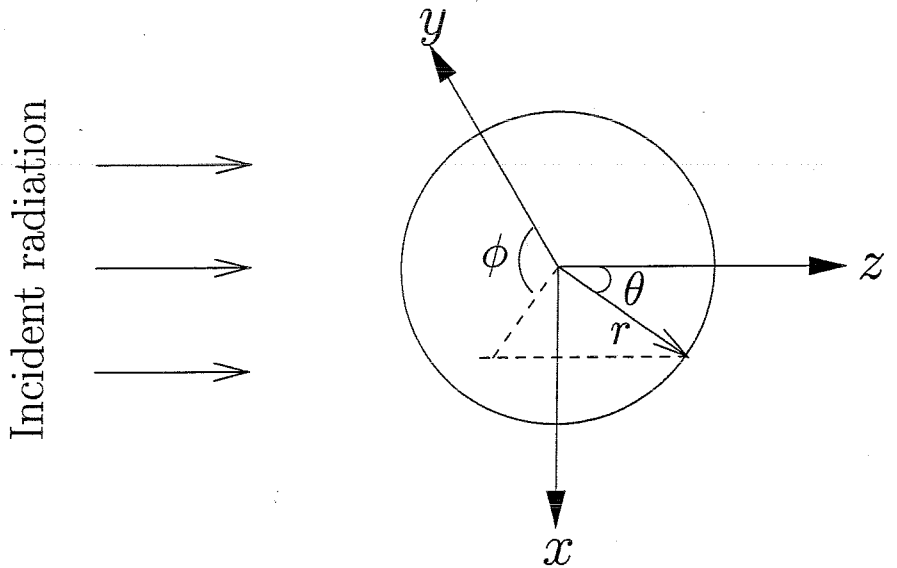


Figure 3.1: Particle-light interaction.

Particle interaction with incident radiation, as illustrated in Figure 3.1, forms the highlight of the present chapter. Matter is composed of discrete electric charges such as electrons and protons. When light is incident on a particle, these charges are set in oscillation where the net effect is manifested in the emission of secondary radiation known as scattering. In addition to scattering, part of the incident radiation may be extinguished within the particle provided that it is absorbing, ie: having a complex index of refraction. Hence, scattering and absorption leads to the temporal implication of reduction of the incident light after traversing a particle. The net effect of radiation extinguished from the incident beam is termed extinction.

In general, the two main formulations for handling particle-light interaction are (i) Mie theory, first

developed by Gustav Mie in 1908 [49], and (ii) ray optics. In the former case, the electromagnetic wave concept is employed and Maxwell's equations are used for the derivation of the incident, scattered and internal fields. These expressions take the form of an infinite series expansion of vector spherical harmonics(VSWF) from which cross sections, efficiency factor and intensity distribution on a particle can be derived. In addition, the effects of particle geometry, particle index with respect to the surrounding medium and angular dependence of the incident beam can be studied. Of particular interest is the feature of structural or morphology-dependent resonance(MDR) where particle resonances are generated by varying the size parameter which is defined as [51]

$$\chi = \frac{2\pi a N_m}{\lambda} , \quad (3.1)$$

where  $a$  denotes the radius of a particle and  $\lambda/N_m$  represents the wavelength in a surrounding medium of index  $N_m$ . The ray model, on the other hand, is based on the concept of light rays traversing a particle resulting in a series of reflections and refractions from which net forces and energies on the particle can be derived [50].

To date, most literature uses the configurations of a plane wave or a Gaussian beam as the incident beam profile. However, in view of the current interest in employing evanescent waves for particle manipulation, much interest has been stimulated in extending the Mie theory to investigate this situation. The first experiment on the interaction of microscopic particles with an evanescent field was performed by Kawata [23] where a 150 mW Nd:YAG source was used to manipulate micron-sized polystyrene and silica particles on the surface of a prism. Shortly after, the experimental results were compared to a theory based on Mie theory developed by Alamaas and Brevik [42]. Very recently, Walz reported on the comparison of Alamaas's and Brevik's results with results from the ray optics approach. He concluded that the latter is only applicable in the limit where  $a > 20\lambda$  [50]. Hence, despite its complexity, Mie theory remains the most complete and reliable model with its applicability extending over the entire range of particle size.

The aims of this theoretical study include an investigations of;

- The morphology-dependent resonance(MDR) of a Mie resonator
- Validity of the Rayleigh approximation applying to latex, gold and silver particles
- Determination of the particle polarizability from the expression of a cross section which relates to optical forces as described later in Chapter 4
- Distribution of the intensity over a cross section of an illuminated particle both in the Rayleigh(ie:  $a < \lambda/N_m$ ) and Mie regimes(ie:  $a > \lambda/N_m$ ) which is useful for applications in fluorescence and Raman sensing
- Comparison of MDR for plane wave and evanescent wave excitation

In the Mie regime, morphology-dependent resonance(MDR) of a dielectric particle has been reported experimentally for example in References [52] and [53]. In the Rayleigh regime where the dipole approximation holds, as described in Section 3.8.1, simplification of the Mie theory allows a straightforward calculation of fields and forces. In this case, particle resonance may originate

from the optical constants of the bulk material. Specifically, resonance occurs when the condition  $\epsilon = -2\epsilon_m$  is satisfied where  $\epsilon$  and  $\epsilon_m$  denote the permittivity of the particle and of the surrounding medium respectively. Hence due to their optical properties, metallic particles such as gold and silver which exhibit strong resonances in the visible region are ideal candidates for the enhancement of Raman signals [2] [3].

In the following sections, the complete analysis of the Mie theory considering the general case of a plane wave excitation is first presented. For simplicity, an x-polarised incident wave with an amplitude  $E_0$  and propagation constant  $\beta_0$  travelling in the  $z$  direction is assumed, which is expressed by

$$\vec{E}_{inc} = E_0 e^{i\beta_0 z} \hat{x} . \quad (3.2)$$

Based on Maxwell's equations and using the wave function, both scalar and vector solutions which subsequently form the field expressions are given in Sections 3.2-3.4. The importance of the radial and angular dependence are evident at this stage. Recurrence relations as highlighted in Section 3.4.2 are crucial for the accurate description of fields particularly when the sphere lies in the Mie regime. Next, the incident, scattered and transmitted fields are presented in Section 3.5.1 and cross sections in Section 3.6, with the Mie scattering and internal coefficients derived by applying the boundary conditions detailed in Section 3.5.2.

After understanding the building blocks behind the Mie theory, the next task is to investigate the cross sections and intensity distribution on a simple, lossless dielectric sphere. The effects of particle radius, absorption and surrounding medium are parameters taken into account. Also, the valid range of the Rayleigh model for latex, gold and silver spheres is given in Section 3.8.2. Finally, the Mie theory is extended for the investigation of the interaction of an evanescent field with a homogeneous sphere as highlighted in Section 3.10. Knowledge of structural-dependent intensity created on a sphere would serve as a valuable tool, for example to the calculation of field enhancement in surface enhanced Raman spectroscopy and fluorescence sensing. In addition, the intensity around a Rayleigh particle is related to its effective polarizability which in turn, affects the optical forces produced as shown later in Chapter 4.

### 3.2 Maxwell's equations

From Maxwell's equations,

$$\nabla \times \vec{E} = i\omega\mu\vec{H} \quad (3.3)$$

$$\nabla \times \vec{H} = -i\omega\mu\vec{E} . \quad (3.4)$$

Taking the curl of 3.3 and 3.4 results in [54]

$$\nabla \times (\nabla \times \vec{E}) = i\omega\mu\nabla \times \vec{H} = \omega^2\epsilon_m\mu\vec{E} \quad (3.5)$$

$$\nabla \times (\nabla \times \vec{H}) = -i\omega\epsilon_m \nabla \times \vec{E} = \omega^2 \epsilon_m \mu \vec{H} . \quad (3.6)$$

By applying the vector identity

$$\nabla \times (\nabla \times \vec{A}) = \nabla(\nabla \cdot \vec{A}) - \nabla \bullet (\nabla \vec{A}) \quad (3.7)$$

results in the time dependent vector wave equations

$$\nabla^2 \vec{E} + k_m^2 \vec{E} = 0 \quad (3.8)$$

$$\nabla^2 \vec{H} + k_m^2 \vec{H} = 0 \quad (3.9)$$

where  $k_m^2 = \omega^2 \epsilon_m \mu$  is the wave vector in the surrounding medium and  $\epsilon_m$  is the permittivity in the surrounding medium. The aim is next to derive the vector solutions of the wave equation. To begin, the following considerations are taken into account [54]:

1. A spherical coordinate system  $(r, \theta, \phi)$  since spherical objects are the subject of interest
2. Defining a scalar function  $\psi_{l,m}$
3. Defining a constant vector  $\vec{r}$  .

Let the scalar function be a solution of

$$\nabla^2 \psi + k_m^2 \psi = 0 . \quad (3.10)$$

In this case, three independent vector solutions can be constructed where [54] [55]

$$\vec{L} = \nabla \psi_{l,m} \quad (3.11)$$

$$\vec{M}_{l,m} = \nabla \times \vec{r} \psi_{l,m} \quad (3.12)$$

and  $\vec{N}_{l,m}$  is related to  $\vec{M}_{l,m}$  via

$$\vec{N}_{l,m} = \frac{1}{k_m} \nabla \times \vec{M}_{l,m} . \quad (3.13)$$

By inspection, Equations(3.8) and (3.9) are satisfied by the vector solutions of  $\vec{L}$ ,  $\vec{M}_{l,m}$  and  $\vec{N}_{l,m}$ . Notice that whilst both  $\vec{M}_{l,m}$  and  $\vec{N}_{l,m}$  are solenoidal functions and are curl of each other, analogous to the relation between  $\vec{E}$  and  $\vec{H}$ ,  $\vec{L}$  represents a purely longitudinal wave and is therefore omitted in this analysis [54].

### 3.3 Scalar solution

In the spherical domain, the scalar solution  $\psi_{l,m}$  in Equation(3.10) is a function of  $R, \theta$  and  $\phi$  which can be expressed by [54] [55] [56]

$$\frac{1}{r^2} \frac{\partial}{\partial r} (r^2 \frac{\partial \psi}{\partial r}) + \frac{1}{r^2 \sin \theta} \frac{\partial}{\partial \theta} (\sin \theta \frac{\partial \psi}{\partial \theta}) + \frac{1}{r^2 \sin^2 \theta} \frac{\partial^2 \psi}{\partial \phi^2} + k_m^2 \psi = 0 \quad (3.14)$$

Next, we seek a particular solution which takes the form of

$$\psi(r, \theta, \phi) = R(r)\Theta(\theta)\Phi(\phi) \quad (3.15)$$

By a separation of variables, the p.d.e function can be transformed to o.d.e. as usual. Defining  $m$  and  $Q$  as the separation constants, the three components and their solutions are [54] [55] [56]:

(A)

$$\begin{aligned} \frac{d^2\Phi}{d\phi^2} + m^2\Theta &= 0 \\ \therefore \Phi &= e^{\pm im\phi} \end{aligned} \quad (3.16)$$

(B)

$$(1 - \cos^2\theta) \frac{d^2\Theta}{d(\cos\theta)^2} - 2\cos\theta \frac{d\Theta}{d(\cos\theta)} + [Q - \frac{p^2}{(1 - \cos^2\theta)}] = 0 \quad (3.17)$$

By applying  $Q = l(l+1)$ , 3.17 resembles an associated Legendre equation [54] [56] hence, we can write

$$\begin{aligned} \Theta &= P_l^m(\eta) \\ &= \frac{(1 - \eta^2)^{\frac{m}{2}}}{2l!} \frac{d^{l+m}(\eta^2 - 1)^l}{d(\eta)^{l+m}} \end{aligned} \quad (3.18)$$

where  $\eta = \cos\theta$  is assumed. For convenience, we will use the simplified expression of  $P_l^m = P_l^m(\eta)$  throughout.

(C)

$$r^2 \frac{d^2R}{dr^2} + 2r \frac{dR}{dr} + (k_m^2 r^2 - Q^2)R = 0 \quad (3.19)$$

The solution of Equation(3.19) is given by

$$R = \sqrt{\frac{2}{\pi}} Z_l(p) \quad (3.20)$$

where  $p = k_m r$ , while  $Z_l(p)$  represents the radial spherical Bessel  $j_l(p)$  and first order Hankel functions  $h_l(p)$ . The choice of these radial functions are explained as follows: As  $j_l(p)$  exhibits finiteness at the origin, it represents the correct description for both the incident and transmitted fields, whilst as  $h_l(p)$  is infinite in the far field, it corresponds to an outgoing spherical wave pattern for the description of a scattered field.

Based on the solutions in (A), (B) and (C), the full description of the scalar solution can be given as

$$\psi_{l,m}(r, \theta, \phi) = \sqrt{\frac{2}{\pi}} Z_l(k_m r) P_l^m e^{im\phi} \quad (3.21)$$

Note that since Equation(3.16) is proportional to odd  $\sin\theta$  and even  $\cos\theta$  functions, Equation(3.21) can be re-expressed as odd and even functions where

$$\psi_{l,m,e}(r, \theta, \phi) = \sqrt{\frac{2}{\pi}} Z_l(k_m r) P_l^m \frac{\cos}{\sin} m\phi \quad (3.22)$$

The subscripts e and o denote even and odd functions respectively. Equation(3.22) will be used in the expansion of the vector solutions for the derivation of the electric and magnetic field components.

### 3.4 Vector solution

#### 3.4.1 Vector spherical harmonics $\vec{M}_{l,m}$ and $\vec{N}_{l,m}$

Based on Equation(3.12) and using the scalar expression in Equation(3.22), the vector  $\vec{M}_{l,m}$  is re-expressed as

$$\vec{M}_{l,m,\phi} = \nabla \times \hat{r}(r\psi_{l,m,\phi}) \quad (3.23)$$

where the relation  $\vec{r} = \hat{r}r$  has been used. By performing the curl, the resulting even and odd modes for  $\vec{M}_{l,m}$  is [54] [55]

$$\vec{M}_{l,m}(\hat{r}) = 0 \quad (3.24)$$

$$\begin{aligned} \vec{M}_{l,m,\phi} &= \frac{1}{r \sin \theta} \frac{d(r\psi)}{d\phi} \hat{\theta} - \frac{1}{r} \frac{d(r\psi)}{d\theta} \hat{\phi} \\ &= \mp Z_l \frac{P_l^m}{\sin \theta \cos m\phi} \sin m\phi \hat{\theta} - Z_l \frac{dP_l^m}{d\theta} \cos m\phi \hat{\phi}. \end{aligned} \quad (3.25)$$

By the relation in Equation(3.13),  $\vec{N}_{l,m}$  can be obtained as [54] [55]

$$\begin{aligned} \vec{N}_{l,m,\phi} &= \frac{l(l+1)}{k_m r} \psi_{l,m,\phi} \hat{r} + \frac{1}{k_m r} \frac{d(r\vec{M}_{l,m,\phi})}{dr} \hat{\theta} + \frac{1}{k_m r} \frac{d(r\vec{M}_{l,m,\theta})}{dr} \hat{\phi} \\ &= \frac{l(l+1)}{k_m r} Z_l P_l^m \frac{\cos m\phi}{\sin m\phi} \hat{r} + \frac{1}{r} \frac{d(pZ_l)}{dp} \frac{P_l^m}{d\theta} \frac{\cos m\phi}{\sin m\phi} \hat{\theta} \\ &\mp m \frac{1}{p} \frac{d(pZ_l)}{dr} \frac{P_l^m}{\sin \theta \cos m\phi} \hat{\phi}. \end{aligned} \quad (3.26)$$

Note that the radial function  $p$  has to be replaced by  $Np$  where  $N = N_s/N_m$  denotes the index of the sphere relative to the surrounding medium, for the correct description of the internal field.

#### 3.4.2 Recurrence equations and useful relations

In this section, useful recurrence relations of the radial and associated Legendre polynomial functions in the Mie analysis particularly for large spheres are highlighted. Upward recurrence of the radial functions and its derivatives are given by [54] [55] [56]

$$\begin{aligned} Z_{l+1}(p) &= \frac{(2l+1)}{p} j_l(p) - j_{l-1}(p) \\ [j_{l+1}(p)]' &= \frac{1}{l+1} \left[ \frac{l}{2l+1} j_{l-1}(p) - (2l+1) j_l(p) \right] \end{aligned} \quad (3.27)$$

The prime denotes differentiation with respect to its argument. Besides, useful equations of recurrences for the  $\theta$ -dependent associated Legendre polynomials and its derivatives are given as follows:

$$P_{l+1}^m = \frac{1}{l-m+1} [(2l+1) \cos \theta P_l^m - (l+m) P_{l-1}^m] \quad (3.28)$$

$$\frac{m P_l^m}{\sin \theta} = \frac{1}{2 \cos \theta} \left[ P_l^{m+1} + (l(l+1) - m(m-1)) P_l^{m-1} \right] \quad (3.29)$$

$$\frac{dP_l^m}{d\theta} = \frac{1}{2}[(l-m+1)(l+m)P_l^{m-1} - P_l^{m+1}] \quad (3.30)$$

The transformation from  $d/d(\cos \theta)$  to  $d/d\theta$  can be conveniently carried out by using the relation

$$\frac{d}{d\theta} = -\sqrt{1-\eta^2} \frac{d}{d(\cos \theta)} \quad (3.31)$$

Also, negative  $m$  terms in the associated Legendre polynomials can be expressed as positive terms via:

$$P_l^{-m} = (-1)^m \frac{(l-m)!}{(l+m)!} P_l^m \quad (3.32)$$

Generally, in a Mie model, it is common to define two angular-dependent terms where [54] [55] [57]:

$$\Pi_{l,m} = m \frac{P_l^m}{\sin \theta} \quad (3.33)$$

and

$$T_{l,m} = \frac{dP_l^m}{d\theta} \quad (3.34)$$

As an illustration to emphasize the significance of these  $\theta$ -angular functions in the description of

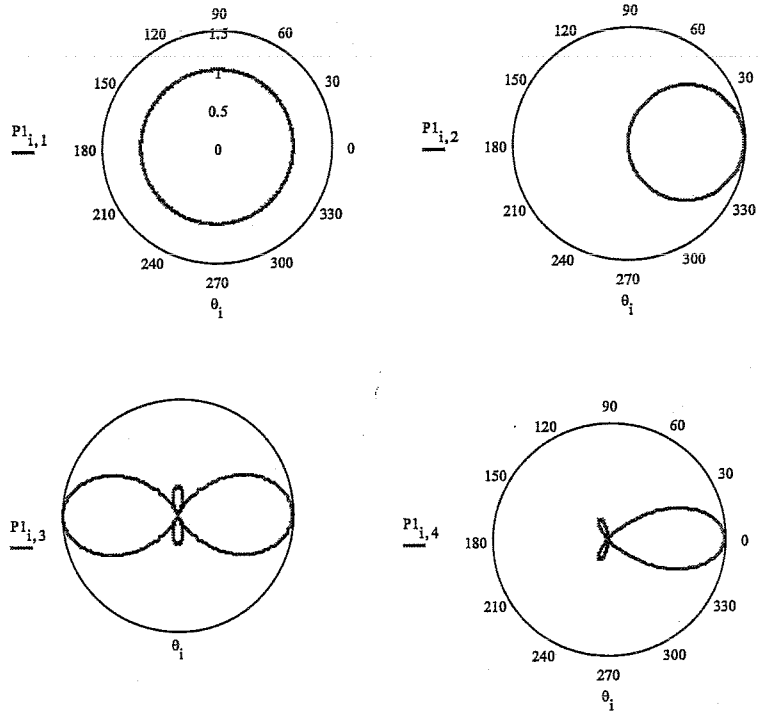


Figure 3.2: Angular  $\theta$ -dependent terms for low order  $l = 1$  to  $4$ .  $m = 1$ .

fields and intensity, the lowest five orders (ie:  $l=1$  to  $l=4$ ) are compared against five higher orders (ie:  $l=15$  to  $l=18$ ) for both  $\Pi_{l,m}$  and  $T_{l,m}$  as denoted by  $P1$  and  $dP2$  respectively in Figures 3.2-3.5 where the first subscript defines the range of angles whilst the second denoted the pole order  $l$  for

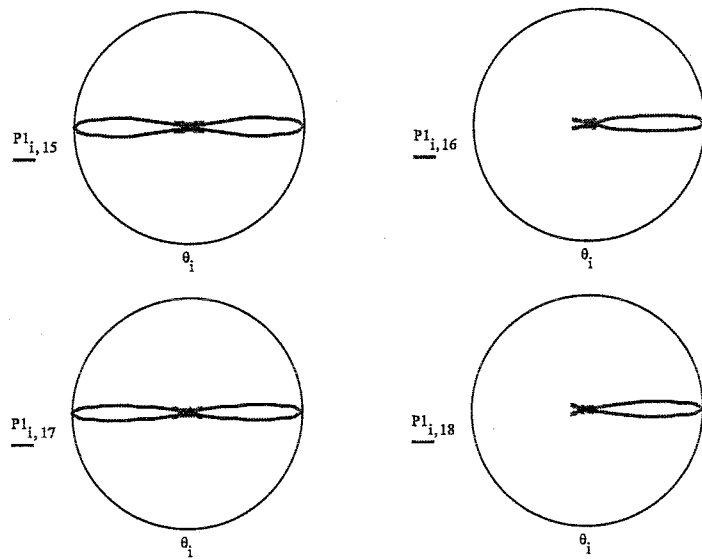


Figure 3.3: Angular  $\theta$ -dependent terms for higher order  $l = 15$  to  $l = 18$  for  $m = 1$ .

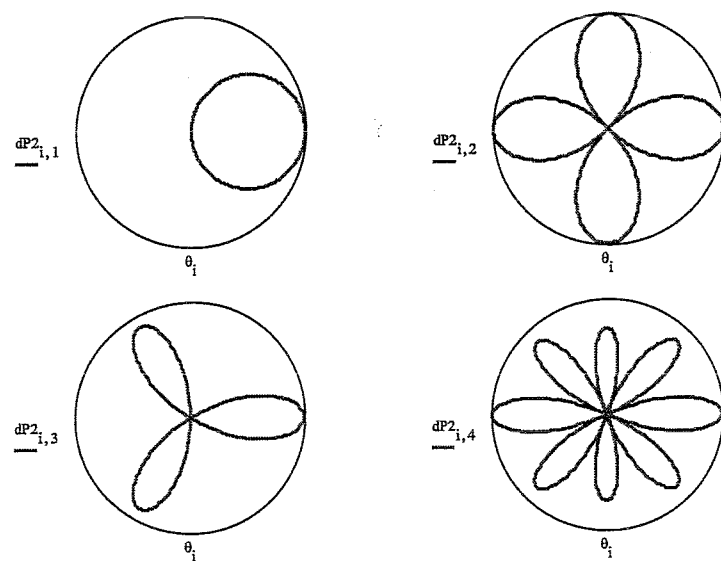


Figure 3.4: Angular  $\theta$ -dependent terms for low order  $l = 1$  to  $4$ .  $m = 1$ .

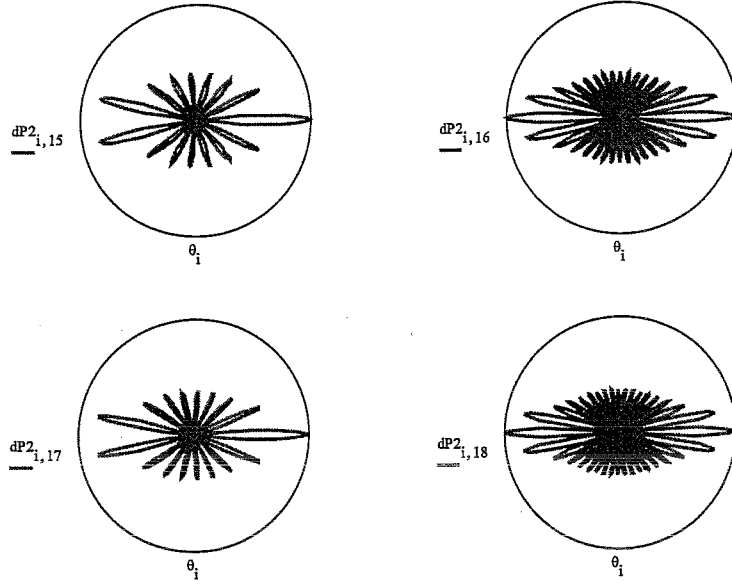


Figure 3.5: Angular  $\theta$ -dependent terms for higher order  $l = 15$  to  $l = 18$  for  $m = 1$ .

each case [55]. These polar plots were obtained by considering  $\theta$  from  $0^\circ$  to  $360^\circ$  and for  $m = 1$  as in a plane wave case [54] [55]. The behaviour of these angular functions will subsequently dictate the variation of intensity distributed around a particle across the range of  $\theta$  [51].

A few points are interestingly noted from these plots:

1. The number of lobes increases as the order  $l$  increases which corresponds to larger spheres.
2. All functions exhibit a forward-directed lobe which is positive in the forward direction. Note that backward lobe vanishes for alternate values of pole order  $l$ . Consequently, forward lobe is enhanced whilst backward lobe is diminished. For a larger sphere, an increasing number of higher order terms of  $\Pi_{l,m}$  and  $T_{l,m}$  are incorporated in the scattering diagram. It is the behaviour of these strongly enhanced forward-directed lobe, compared to backscattering directions which leads to sharper and narrower forward scattered peak as a particle becomes larger, ie: with bigger size parameter  $\chi$  [55].

### 3.5 Incident, scattered and internal fields

#### 3.5.1 Expansion coefficients

It is assumed that an arbitrary wave expressed by a vector potential  $\vec{A}$  can be represented by a linear combination of characteristic vector functions where [54]

$$\vec{A} = \frac{i}{\omega} \sum_{l,m} [A_{l,m} \vec{M}_{l,m} + B_{l,m} \vec{N}_{l,m}] . \quad (3.35)$$

As mentioned earlier,  $\vec{M}_{l,m}$  and  $\vec{N}_{l,m}$  are included as they represent solenoidal functions corresponding to the nature of the dependence between the electric and magnetic fields. On the other hand,  $\vec{L}_{l,m}$  is omitted in Equation(3.35) as it represents a longitudinal field. Hence, by rearranging Equation(3.3) and using  $\vec{A}$ , the magnetic field can be expressed as

$$\begin{aligned}\vec{H}_{inc} &= \frac{1}{i\omega\mu} \nabla \times \vec{A} \\ &= -\frac{i}{\omega\mu} \sum [A_{l,m}(\nabla \times \vec{M}_{l,m}) + B_{l,m}(\nabla \times \vec{N}_{l,m})] \\ &= -\frac{ik_m}{\omega\mu} \sum [A_{l,m} \vec{N}_{l,m} + B_{l,m} \vec{M}_{l,m}] .\end{aligned}\quad (3.36)$$

Similarly, using Equations(3.4) and (3.36), the incident electric field can be written as

$$\vec{E}_{inc} = \frac{k_m}{\omega^2 \epsilon_m \mu} \sum [A_{l,m} \vec{M}_{l,m} + B_{l,m} \vec{N}_{l,m}] .\quad (3.37)$$

The notations  $A_{l,m}$  and  $B_{l,m}$  are the expansion coefficients which are characteristic for a particular incident beam, which can be derived by considering

$$\begin{aligned}A_{l,m} &= \int M_{l,m}^* \vec{E}_{inc} d\Omega \\ B_{l,m} &= \int N_{l,m}^* \vec{E}_{inc} d\Omega\end{aligned}\quad (3.38)$$

where  $\Omega = 4\pi r^2$  is the surface area enclosed. The resulting expressions are [55]

$$A_{l,m} = -i^{l+1} \frac{2l+1}{l(l+1)} \frac{(l-m)!}{(l+m)!} \Pi_{l,m} E_0 \quad (3.39)$$

and

$$B_{l,m} = -i^{l+2} N_m \frac{2l+1}{l(l+1)} \frac{(l-m)!}{(l+m)!} T_{l,m} E_0 .\quad (3.40)$$

where  $E_0$  represents the field amplitude. The equations above are the general expression which may take a simplified form when considering a particular wave profile. For example, for a plane wave where the incident angle  $\theta = 0$  and all terms vanish except for  $m = 1$  [54] [55]. Based on Equations(3.29) and (3.30),  $\Pi_{l,1} = 1$  and

$$T_{l,1} = \frac{1}{2} l(l+1) .\quad (3.41)$$

Also, since

$$\frac{1}{l(l+1)} \frac{(l-1)!}{(l+1)!} = \frac{1}{[l(l+1)]^2} ,\quad (3.42)$$

a much simplified expression for the expansion coefficients in the case of plane wave excitation can be expressed as

$$A_{l,1} = i^{l-1} E_0 \frac{2l+1}{l(l+1)} .\quad (3.43)$$

and  $B_{l,1} = i A_{l,1}$ . It is now clear from a comparison of Equation(3.39) and Equation(3.43) that more resonances may be excited by an incident evanescent wave where more angular terms are

incorporated in the scattering and internal fields. Note that both the electric and magnetic field are expressed in terms of the vector solutions  $\vec{M}_{l,m}$  and  $\vec{N}_{l,m}$  while many authors have replaced it with the vector  $\vec{X}_{l,m}$  where they are related by [58]

$$\vec{M}_{l,m} = -i\sqrt{\frac{4\pi l(l+1)}{2l+1}\frac{(l+m)!}{(l-m)!}}Z_l\vec{X}_{l,m} \quad (3.44)$$

In a same way, the scattered and internal fields are given as [55]

$$\begin{aligned} \vec{E}_{scat} &= \frac{k_m}{\omega^2 \epsilon_m \mu} \sum [A_{l,m} a_l \vec{M}_{l,m} + B_{l,m} b_l \vec{N}_{l,m}] \\ \vec{H}_{scat} &= -\frac{ik_m}{\omega \mu} \sum [A_{l,m} a_l \vec{N}_{l,m} + B_{l,m} b_l \vec{M}_{l,m}] \\ \vec{E}_{int} &= \frac{k_m}{\omega^2 \epsilon_m \mu} \sum [A_{l,m} c_l \vec{M}_{l,m} + B_{l,m} d_l \vec{N}_{l,m}] \\ \vec{H}_{int} &= -\frac{ik_m}{\omega \mu} \sum [A_{l,m} c_l \vec{N}_{l,m} + B_{l,m} d_l \vec{M}_{l,m}] \end{aligned} \quad (3.45)$$

where  $a_l$  and  $b_l$  are the scattering coefficients,  $c_l$  and  $d_l$  are coefficients of the internal fields. The permittivity of the surrounding medium and of the particle are denoted by  $\epsilon_m$  and  $\epsilon$  respectively. These expressions are obtained from the boundary conditions which are explained in the following section.

### 3.5.2 Determination of Mie coefficients from the boundary conditions

Mie coefficients  $a_l$ ,  $b_l$ ,  $c_l$  and  $d_l$  which form the expansion of the scattered and internal fields respectively in a particle can be determined from the boundary conditions described as follows.

Electromagnetic fields are required to satisfy Maxwell's equations in regions where the permittivity and the permeability are isotropic and constant. However, as one crosses the boundary of a particle embedded in a medium, these properties are abruptly altered. This change occurs over a transition region with thickness of the order of atomic dimensions. At such boundaries, the following conditions are imposed where the tangential components of  $\vec{E}$  and  $\vec{H}$  are continuous across the boundary separating the two media

$$\begin{aligned} [\vec{E}_{inc} + \vec{E}_{scat} - \vec{E}_{int}] \times \vec{r} &= 0 \\ [\vec{H}_{inc} + \vec{H}_{scat} - \vec{H}_{int}] \times \vec{r} &= 0 \end{aligned} \quad (3.46)$$

Hence,

$$E_{inc,\theta} + E_{scat,\theta} = E_{int,\theta} \quad H_{inc,\theta} + H_{scat,\theta} = H_{int,\theta} \quad (3.47)$$

$$E_{inc,\phi} + E_{scat,\phi} = E_{int,\phi} \quad H_{inc,\phi} + H_{scat,\phi} = H_{int,\phi} \quad (3.48)$$

which upon applying the vector spherical harmonics results in four equations where

$$\begin{aligned} j_l(N\chi)c_l + h_l(\chi)b_l &= j_l(\chi) \\ [N\chi j_l(N\chi)]'c_l + [\chi h_l(\chi)]'b_l &= [\chi j_l(\chi)]' \\ Nj_l(N\chi)d_l + h_l(\chi)a_l &= j_l(\chi) \\ [N\chi j_l(N\chi)]'d_l + N[\chi h_l(\chi)]'a_l &= N[\chi j_l(\chi)]' \end{aligned} \quad (3.49)$$

evaluated at  $r = a$ . Solving Equation(3.49) leads to the following well known expressions of the Mie coefficients where the scattering coefficients  $a_l$ ,  $b_l$  and coefficients of an internal field  $c_l$ ,  $d_l$  are [54] [55] [57]

$$\begin{aligned} a_l &= \frac{N^2 j_l(N\chi)[\chi j_l(\chi)]' - j_l(\chi)[N\chi j_l(N\chi)]'}{N^2 j_l(N\chi)[\chi h_l(\chi)]' - h_l(\chi)[N\chi j_l(N\chi)]'} \\ b_l &= \frac{j_l(N\chi)[\chi j_l(\chi)]' - j_l(\chi)[N\chi j_l(N\chi)]'}{j_l(N\chi)[\chi h_l(\chi)]' - h_l(\chi)[N\chi j_l(N\chi)]'} \\ c_l &= \frac{j_l(\chi)[\chi h_l(\chi)]' - h_l(\chi)[\chi j_l(\chi)]'}{j_l(N\chi)[\chi h_l(\chi)]' - h_l(\chi)[N\chi j_l(N\chi)]'} \\ d_l &= \frac{Nj_l(\chi)[\chi h_l(\chi)]' - Nh_l(\chi)[\chi j_l(\chi)]'}{N^2 j_l(N\chi)[\chi h_l(\chi)]' - h_l(\chi)[N\chi j_l(N\chi)]'} \end{aligned} \quad (3.50)$$

Note that these expressions diverge as their denominator vanishes. When this occurs, the fields which are expressed as an infinite series of these coefficients exhibit resonance peaks. Occurrence of such peaks, as evident from Equation(3.50), would strongly depend on the size of the particle, which is the reason they are termed structural or morphology-dependent resonances(MDR). Other factors that influence the behaviour of these coefficients are the indices  $N_s$  and  $N_m$  of the sphere and surrounding medium respectively, and the incident wavelength. Examples of the behaviour of these coefficients are given in later sections both for a lossless and for a lossy sphere.

### 3.6 Extinction and scattering cross sections

By applying the complex Poynting vector law, the net rate of change of energy as light traverses the particle can be determined. Subsequently, both the scattered and extinction cross sections in  $\text{m}^2$  can be obtained using the relations [55]:

$$C_{scat} = \frac{W_{scat}}{I_{inc}} \quad (3.51)$$

$$C_{ext} = \frac{W_{ext}}{I_{inc}} \quad (3.52)$$

where  $I_{inc}$  represents the intensity incident on the surface of the particle.  $W_{scat}$  and  $W_{ext}$  are the scattered and extinction energies given respectively by [55]:

$$\begin{aligned} W_{scat} &= \frac{1}{2} \operatorname{Re} \int_0^{2\pi} \int_0^\pi (E_{scat} \times H_{scat}^*) r^2 \sin\theta d\theta d\phi \\ &= \frac{1}{2} \operatorname{Re} \int_0^{2\pi} \int_0^\pi (E_{scat,\theta} \times H_{scat,\phi}^* - E_{scat,\phi} \times H_{scat,\theta}^*) r^2 \sin\theta d\theta d\phi \end{aligned} \quad (3.53)$$

$$\begin{aligned}
W_{ext} &= \frac{1}{2} \operatorname{Re} \int_0^{2\pi} \int_0^\pi (E_{inc} \times H_{scat}^*) r^2 \sin\theta d\theta d\phi \\
&= \frac{1}{2} \operatorname{Re} \int_0^{2\pi} \int_0^\pi (E_{inc,\phi} \times H_{scat,\theta}^* - E_{inc,\theta} \times H_{scat,\phi}^* \\
&\quad - E_{scat,\theta} \times H_{inc,\phi}^* + E_{scat,\theta} \times H_{inc,\phi}^*) r^2 \sin\theta d\theta d\phi
\end{aligned} \tag{3.54}$$

The absorbed energy can be related to the scattered and extinction energies by  $W_{ab} = W_{ext} - W_{scat}$ . By applying Equations(3.53) and (3.54) into Equations(3.51) and (3.52), one can arrive at [59] [60]

$$C_{scat} = \frac{2\pi}{k_m^2} \sum_{l=1}^{\infty} (2l+1)(a_l |H_{l,m}|^2 + b_l |F_{l,m}|^2) \tag{3.55}$$

and

$$C_{ext} = \frac{2\pi}{k_m^2} \operatorname{Re} \sum_{l=1}^{\infty} (2l+1)(a_l |H_{l,m}|^2 + b_l |F_{l,m}|^2) \tag{3.56}$$

for the scattered and extinction cross sections respectively. Angular functions  $F_{l,m}$  and  $H_{l,m}$  are related to  $\Pi_{l,m}$  and  $T_{l,m}$  by

$$F_{l,m} = \frac{2}{l(l+1)} \sum_{m=-l}^l \frac{(l-m)!}{(l+m)!} |\Pi_{l,m}|^2 \tag{3.57}$$

and

$$H_{l,m} = \frac{2}{l(l+1)} \sum_{m=-l}^l \frac{(l-m)!}{(l+m)!} |T_{l,m}|^2 \tag{3.58}$$

For plane wave excitation where all terms vanish except for  $m = 1$ , Equations (3.55) and (3.56) reduce to [55] [57]

$$C_{scat} = \frac{2\pi}{k_m^2} \sum_{l=1}^{\infty} (2l+1)(|a_l|^2 + |b_l|^2) \tag{3.59}$$

and

$$C_{ext} = \frac{2\pi}{k_m^2} \operatorname{Re} \sum_{l=1}^{\infty} (2l+1)(a_l + b_l) \tag{3.60}$$

Again, the equations stress the point that for an evanescent wave where  $\theta > 0$ , more angular terms contribute to the final cross sections, which results in the excitation of more resonant modes [44] [59] [60] [62].

A term which is associated with cross section is the dimensionless parameter commonly known as efficiency factor or Q-factor. The extinction and scattering efficiencies are given respectively by [55]

$$\begin{aligned}
Q_{ext} &= \frac{C_{ext}}{G} \\
Q_{scat} &= \frac{C_{scat}}{G}
\end{aligned} \tag{3.61}$$

where  $G$  defines the geometrical cross section which is  $\pi a^2$  for a sphere or particle radius  $a$ .

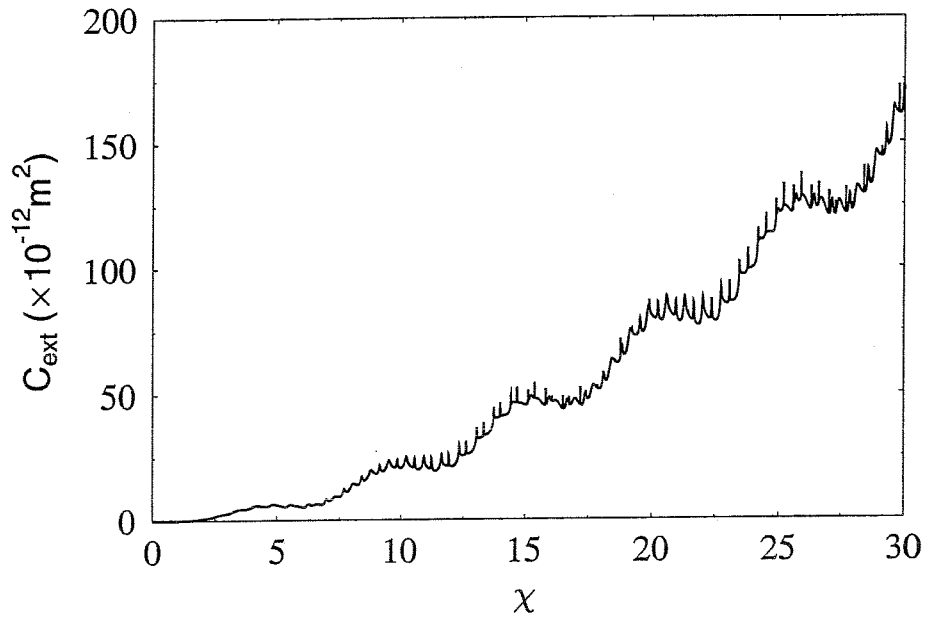


Figure 3.6: Extinction cross section for a latex sphere with an index of  $N_s = 1.59$  in air,  $\lambda = 1\mu\text{m}$ .

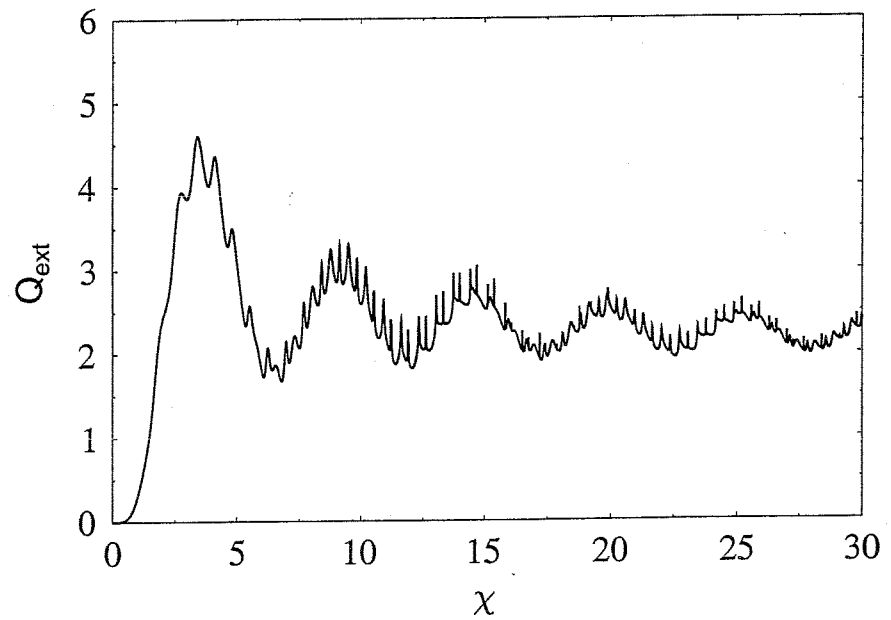


Figure 3.7: Extinction efficiency for a latex sphere with an index of  $N_s = 1.59$  in air,  $\lambda = 1\mu\text{m}$ .

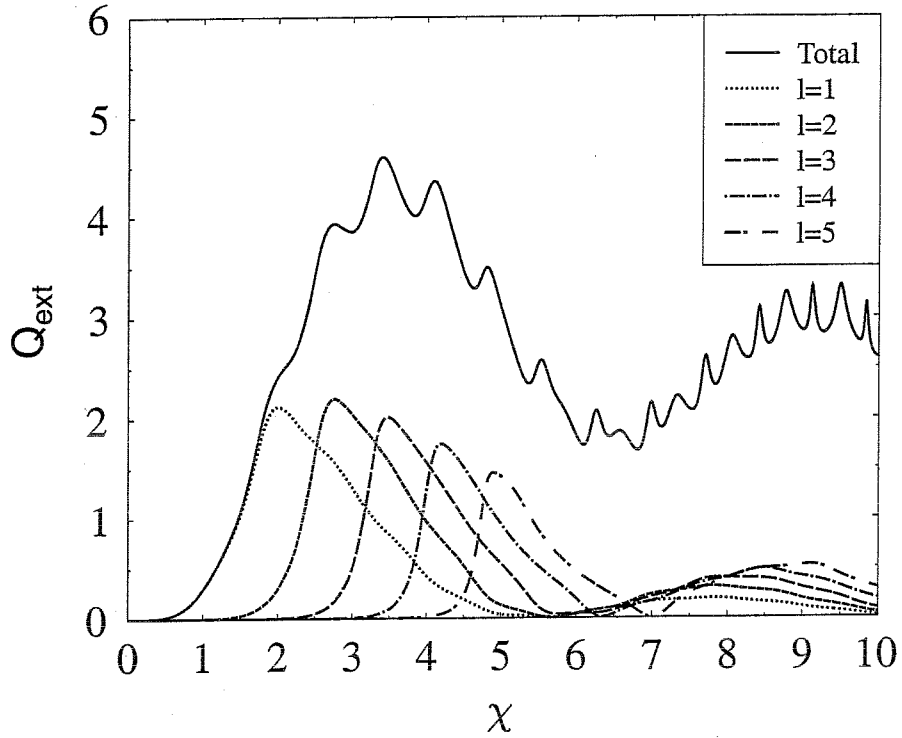


Figure 3.8: Contribution from the first five poles of  $l = 1$  to  $l = 5$  for a latex sphere in a range of small size parameter.

### 3.7 Resonances of a dielectric sphere

In this section, the behaviour of a dielectric particle is used to illustrate structural-dependent resonances in a Mie resonator. For comparison with later experiments discussed in Chapter 7, a latex sphere of index 1.59 is chosen. In the first instance, a lossless latex particle with zero imaginary part of index is assumed implying that extinction is solely caused by scattering.

#### 3.7.1 Multipole series expansion

For simplicity, consider excitation by a plane wave with air as the surrounding medium. Using Equations(3.56) and (3.61), the variation of both the extinction cross section and efficiency for a latex sphere with a size parameter ranging from  $\chi = 0$  to  $\chi = 30$  obtained with a resolution of  $\Delta\chi = 10^{-3}$  and a total of 40 poles(ie:  $l = 40$ ), are shown in Figure 3.6 and Figure 3.7 respectively. In this case, an incident plane wave at a wavelength of  $1\mu m$  is considered with the size parameter determined by varying the particle radius. For the purpose of illustration, the two extremes of the spectral in  $Q_{ext}$  have been enlarged, as shown in Figure 3.8 for  $\chi < 10$ , and in Figure 3.9 for the range of  $\chi = 12$  to  $\chi = 20$ . In addition, the contribution from individual poles of  $l = 18$ ,  $l = 19$ ,  $l = 20$  and  $l = 25$  is shown on these plots to emphasize the origin of the corresponding spectral

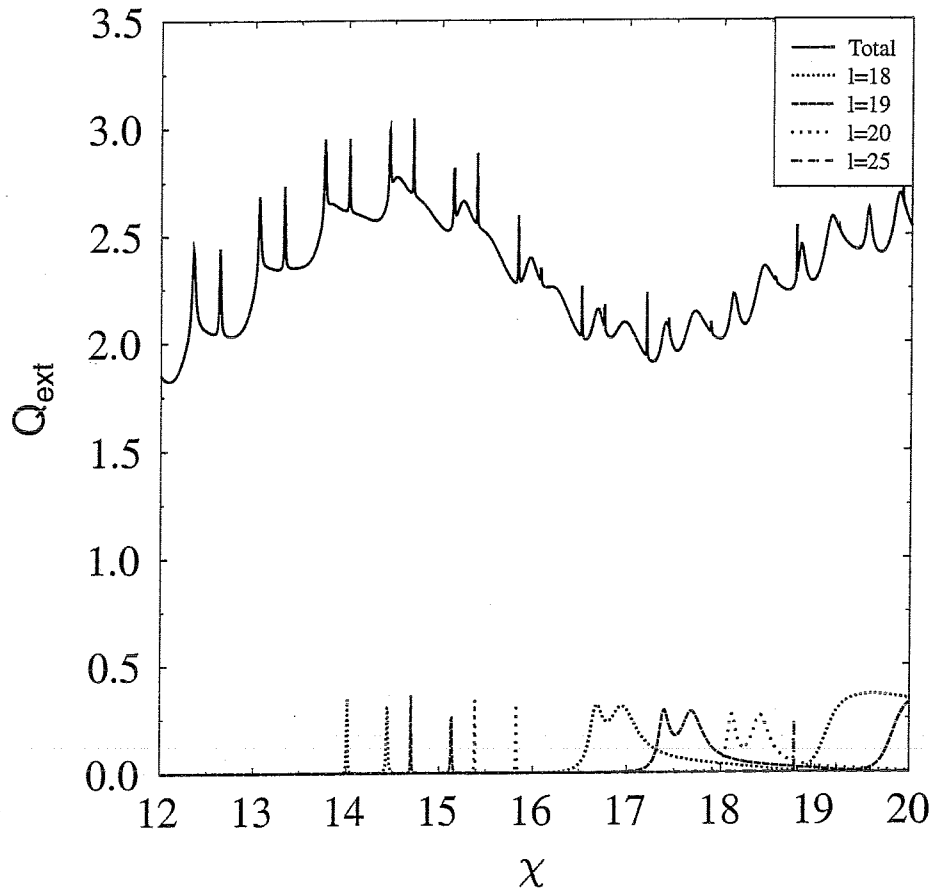


Figure 3.9: Superimposed pole contribution to extinction efficiency of a latex sphere with an illustration of contribution from pole orders of  $l = 18, 19, 20$  and  $l = 25$ .

features generated. The reason for selecting a pole order of  $l = 25$  is to relate it to the intensity distribution around a latex sphere of radius  $3\mu\text{m}$  later in Section 3.9.

The following features are highlighted:

1. The spectral response is a direct result of superposition from individual poles  $l$ . For example, based on Figure 3.9, an intense resonant line for a size parameter of  $\chi = 14$  and  $\chi = 18.85$  arises from a pole order of  $l = 18$  and  $l = 25$  respectively.
2. For small size parameter, the effect due to Rayleigh scattering is evident which is identified by the broadened spectral as shown in the expanded section in Figure 3.8.
3. The most striking feature, however, is the existence of a ripple structure, which emerges as the size parameter increases, ie: for large spheres. This is shown in Figure 3.9. Each of these peaks is important as it implies high energy storage within the particle. In practical terms,

lower incident intensities would be required to manipulate a particle at resonance [51] [52] [53]. Information such as these may provide a means for example to identify a specific particle for sorting purposes or in surface enhancement of fields for fluorescence and Raman excitation.

4. In Figure 3.9, the contribution from each pole  $l$  shows the appearances of an intense peak and subsequent higher order structures which rapidly broaden as the size parameter increases. Specifically, for a pole of order  $l = 18$ , the first order peak appears at  $\chi = 14$  which by inspection represents a very narrow structure corresponding to the peak in  $Q_{ext}$ . The second order peak corresponding to this pole is slightly broadened and emerges at  $\chi = 14.4$  which coincides with  $Q_{ext}$  in the same way as before. Finally, a much broadened feature starts to appear at  $\chi = 16.75$  for this pole. The effect of superposition of all poles explains the zero offset as evident on the cross section and extinction plots in Figure 3.6 and Figure 3.7 respectively.

Hence, the contribution of individual pole to the ripple structure in an extinction efficiency spectral has been understood. To gain further insight into the physical origin of the resonances, the behaviour of the Mie coefficients is studied next.

### 3.7.2 Origin of morphology-dependent resonance(MDR)

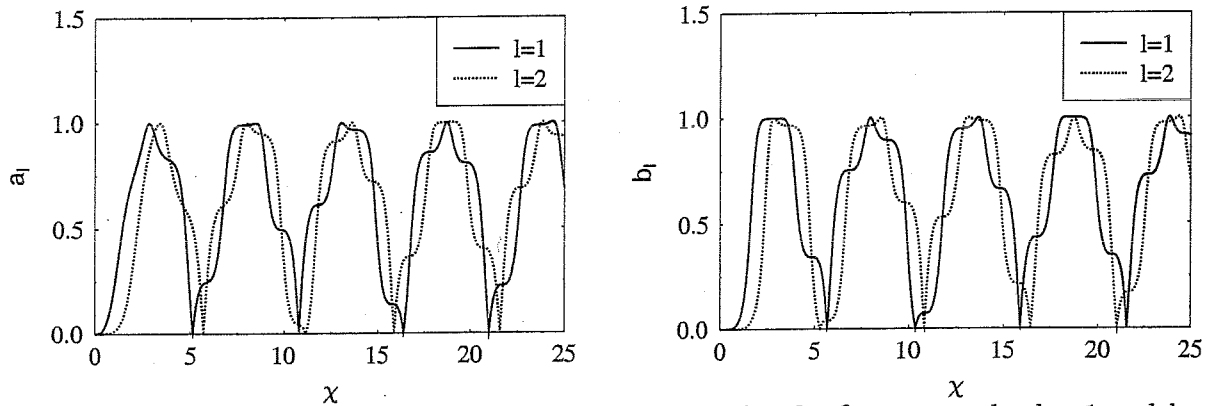


Figure 3.10: Mie scattering coefficients,  $a_l$  and  $b_l$ , for the first two poles  $l = 1$  and  $l = 2$ .

By inspection of Equation(3.50), resonant peaks shown previously in Figure 3.6, Figure 3.7 and Figure 3.9 find their origin in the behaviour of the radial Bessel and Hankel functions and their derivatives which are incorporated in the Mie coefficients. Accordingly, resonance occurs when the denominator of the Mie coefficients approaches zero, ie:

$$N^2 \frac{j_l(N\chi)}{[N\chi j_l(N\chi)]'} = \frac{h_l(\chi)}{[\chi h_l(\chi)]'} \quad (3.62)$$

or when

$$\frac{j_l(N\chi)}{[N\chi j_l(N\chi)]'} = \frac{h_l(\chi)}{[\chi h_l(\chi)]'} \quad (3.63)$$

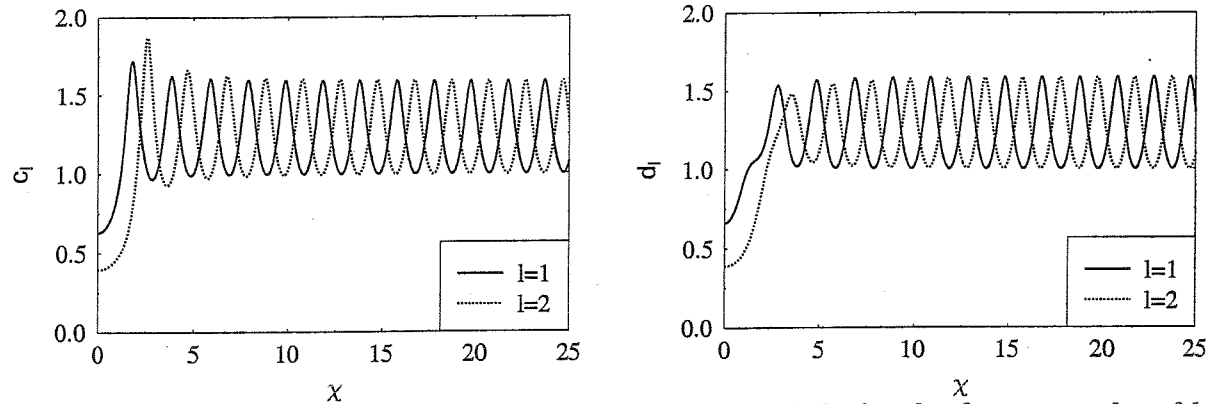


Figure 3.11: Mie coefficients of an internal field,  $c_l$  and  $d_l$ , for the first two poles of  $l = 1$  and  $l = 2$ .

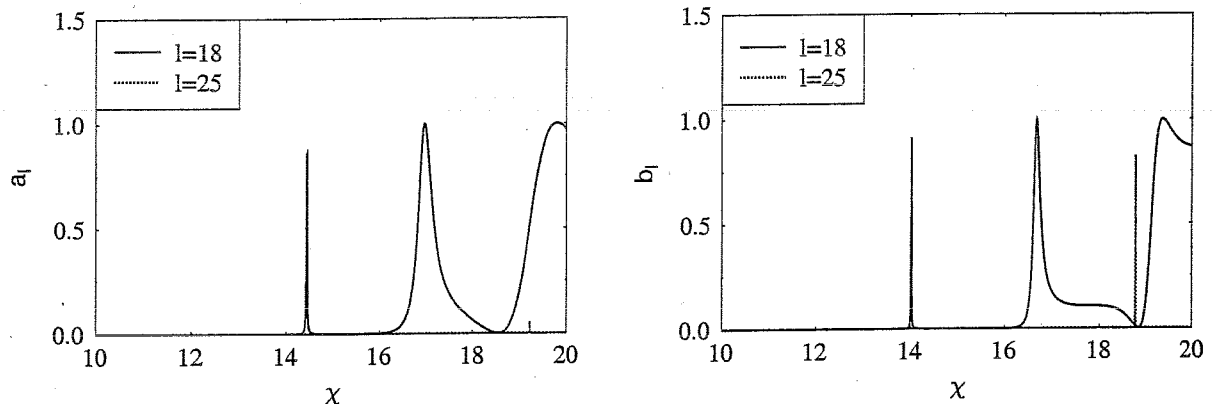


Figure 3.12: Mie scattering coefficients,  $a_l$  and  $b_l$ , for poles  $l = 18$  and  $l = 25$  respectively.

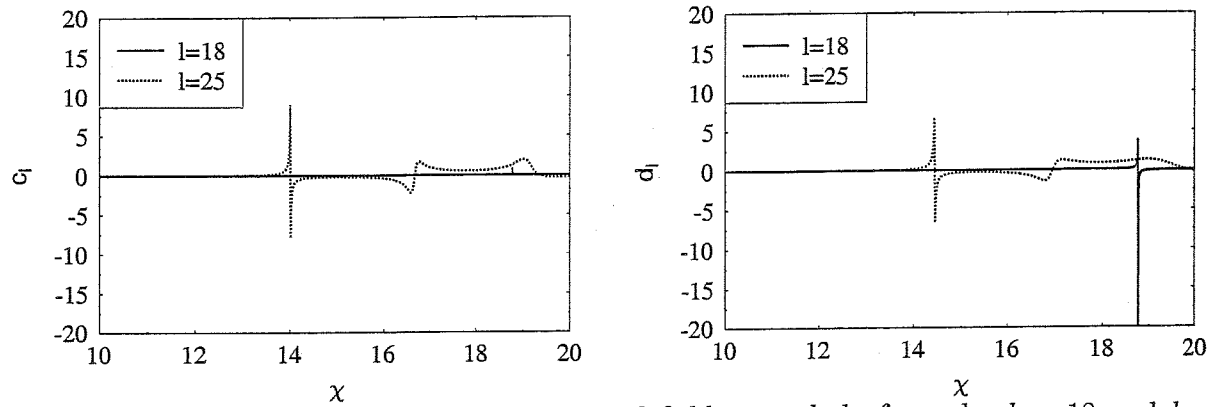


Figure 3.13: Mie coefficients of an internal field,  $c_l$  and  $d_l$ , for poles  $l = 18$  and  $l = 25$  respectively.

To illustrate their behaviour, the scattering coefficients  $a_l$ ,  $b_l$  and coefficients of the internal field  $c_l$  and  $d_l$  are shown in Figures 3.10-3.11 for the lowest two pole orders  $l = 1$  and  $l = 2$ . By inspection, the spectral corresponding to these low order poles are much broader, in agreement with a similar feature in the  $Q_{ext}$  spectral for a size parameter of  $\chi < 5$  as shown in Figure 3.8. As a comparison, higher pole orders corresponding to  $l = 18$  and  $l = 25$  are shown in Figures 3.12-3.13. A stark difference is observed as the pole order increases which relates to the appearance of more intensely narrow peaks. The coincidence of the structures contained in  $a_l$  and  $b_l$  with the extinction cross section and efficiency at specific  $\chi$  values is readily observed.

By inspection, whilst a strong resonant feature exhibited by  $Q_{ext}$  for a size parameter of  $\chi = 14$  originates from  $b_l$ , the peak at  $\chi = 14.4$  is due to  $a_l$ , both corresponding to a first order pole of  $l = 18$ . The manner in which the Mie coefficients selectively enhance a particular mode is evident across the entire  $Q_{ext}$  spectral range. Due to this behaviour exhibited by the Mie coefficients, they are known as partial wave coefficients where the combined effect is manifested in the resultant wave pattern [51]. Very often, Mie coefficient are appended with a subscript and a superscript where the former indicates the pole order while the latter represents the order of appearance of a resonant mode for a particular pole. As an illustration based on Figure 3.12, the scattering coefficients are denoted by  $a_{18}^1$ ,  $a_{18}^2$ ,  $a_{18}^3$  and  $b_{18}^1$ ,  $b_{18}^2$ ,  $b_{18}^3$ , in accordance to an increase in the appearance of the respective enhance feature with increasing  $\chi$ . Hence, the resonant mode corresponding to a pole order of  $l = 18$  in  $Q_{ext}$  is excited by a partial wave coefficient relating to  $b_{18}^1$ . Finally, notice that by a comparison of Figure 3.12 and Figure 3.13, the internal coefficients  $c_l$  and  $d_l$  are ten times stronger than the scattering coefficients, which implies that a larger resonant effect can be generated within a larger latex sphere.

Let us try to understand from the point of view of a ray picture. When light interacts with a particle, rays undergo multiple internal reflections within it, analogous to the case in a one dimensional Fabry-Perot. Constructive interference is therefore the origin of these resonances [61]. Also, the bigger the sphere, the larger the number of reflections. This implies a smaller reflection angle resulting in very sharp resonant modes as shown by the sharp structure corresponding to higher orders of the Mie coefficients in Figures 3.12 and 3.13 [61]. This also explains the much broader structure evident in a small sphere. However, excitation of these resonant modes strongly depends on the incident beam, in particular, its symmetry. For instance, due to the non-vanishing angular terms in the expressions for Gaussian and evanescent wave excitation which leads to higher intensity gradient, more internal resonant modes can be excited. Excellent examples of the latter were given by Chew, Liu and Quinten [44, 59, 60, 62]. On the other hand, in the case where phase matching condition is achieved at the boundary of the particle, an internal ray is expected to be transmitted out of a particle contributing to a series of scattered rays [51].

### 3.7.3 The effect of surrounding medium and absorption

For the same latex sphere considered in Sections 3.7.1 and 3.7.2, plots of extinction efficiency for a range of increasing surrounding index  $N_m = 1, 1.1, 1.2$  and  $N_m = 1.33$  are shown in Figure 3.14. When the index of the surrounding medium is changed, behaviour of particle resonance is affected.

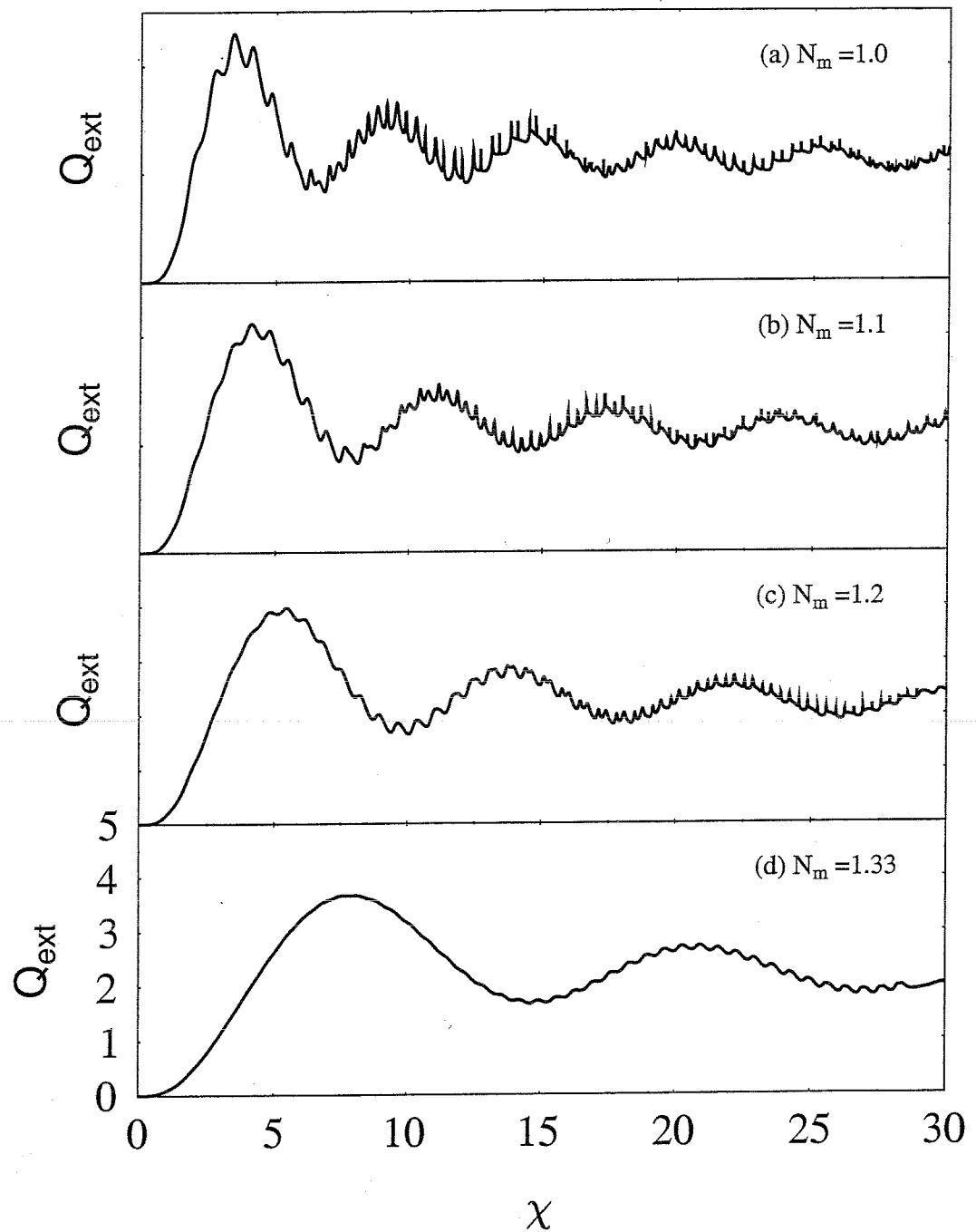


Figure 3.14: Extinction efficiency of latex sphere  $N_s = 1.59$  in a range of surrounding media,  $\lambda = 1\mu\text{m}$ . The scale for figures (a)-(c) follows that of (d).

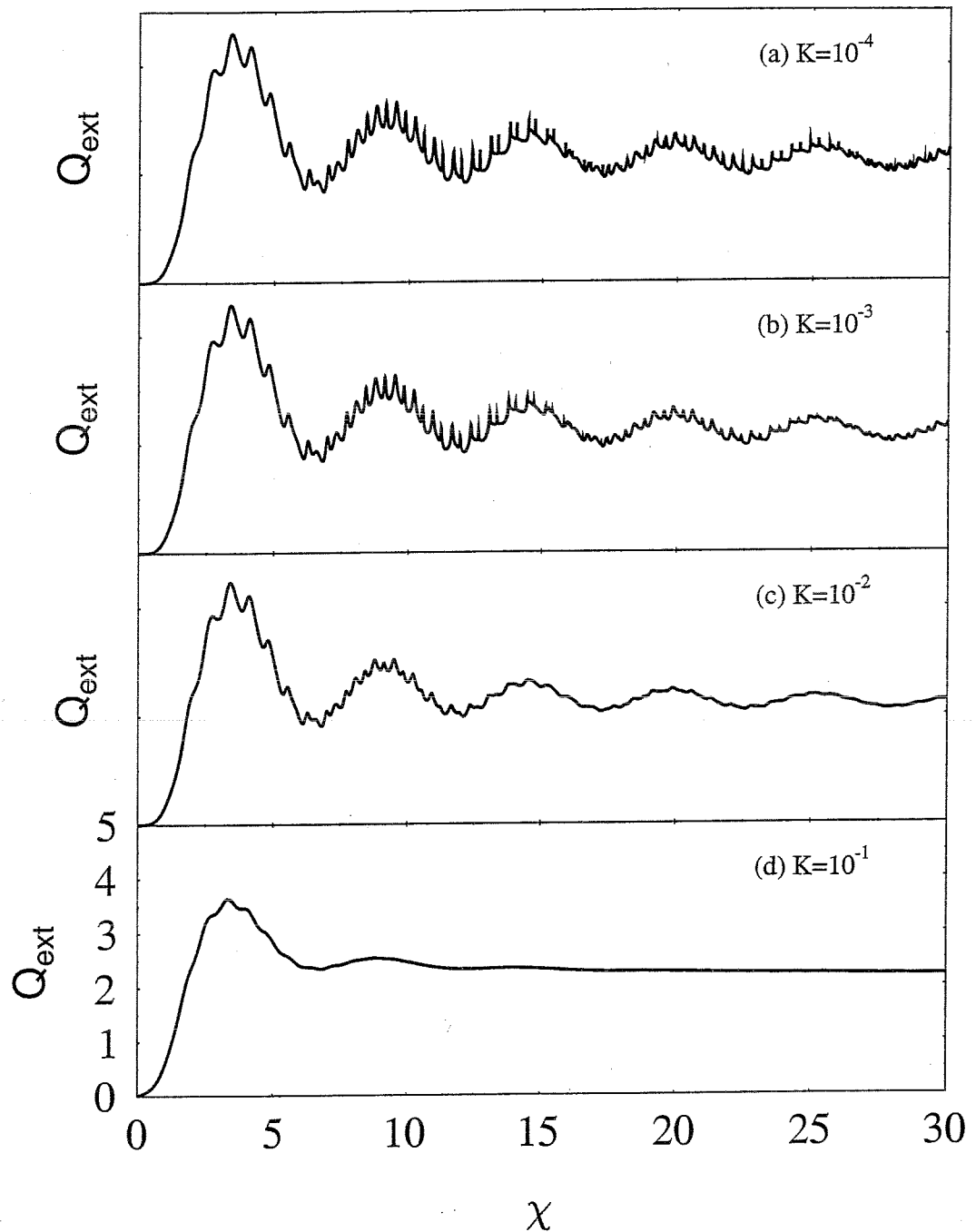


Figure 3.15: Extinction efficiency of latex sphere  $N_s = 1.59$  for a range of imaginary part of index in air,  $\lambda = 1\mu\text{m}$ . The scale for figures (a)-(c) is the same as (d).

Specifically, when the index in the surrounding medium  $N_m$  is increased, light becomes increasingly weakly confined in the particle which results in less light scattered and absorbed by a particle. A direct effect is the damping of resonances leading to broadened features. The reason for choosing index  $N_m = 1.33$  which corresponds to a water medium is due to its practical importance. It is obvious from Figure 3.14 that the extinction spectrum is increasingly 'smoothed out' with a larger  $N_m$ . In particular, strong damping is shown in the case for water  $N_m = 1.33$  where most of the fine structure is reduced in comparison to that in a higher index surrounding medium. Note that in all cases, the resonance becomes increasingly sharper as the size parameter increases either by using a larger particle or by decreasing the incident wavelength [63] [64].

Another way of dampening optical resonances in a particle is by introducing a small absorption into the particle. Four examples corresponding to an increase in absorption coefficient of  $K = 10^{-4}, 10^{-3}, 10^{-2}$  and  $10^{-1}$  for a latex sphere are shown in Figure 3.15. For a small absorption region, where  $K = 10^{-4}$  in Figure 3.15(d) and  $K = 10^{-3}$  in Figure 3.15(c), resonances remain strongly evident. However, as  $K$  is increased to a value of  $10^{-2}$  in Figure 3.15(b), the sharp peaks become strongly damped. For a strongly absorbing particle with  $K = 10^{-1}$ , as shown in Figure 3.15(a), note that it no longer supports any observable structural resonances and the spectrum is significantly smoothed out for  $\chi > 10$ .

Hence, a conclusion to be drawn here is that MDR is enhanced for a particle exhibiting a small absorption coefficient and a maximum index difference with respect to the surrounding medium.

## 3.8 The Rayleigh approximation for small particles

### 3.8.1 Derivation of Rayleigh cross sections

By considering a latex sphere in air, we compare the Mie extinction cross section and the contribution from the two lowest pole orders (ie:  $l = 1, 2$ ). As evident on Figure 3.16, the main contributor to the net extinction cross section of a Rayleigh sphere, ie:  $\chi < 1$ , comes from the lowest order pole, ie:  $l = 1$ . Hence, higher order terms can be omitted in this case. The expression of the  $j_l$  and  $h_l$  can be written in series form which by extracting the lowest order term (ie:  $l = 1$ ) leads to [55]

$$\begin{aligned} \chi j_1 &= \frac{\chi^2}{3} - \frac{\chi^4}{30} \\ [\chi j_1]' &= \frac{2\chi}{3} - \frac{2\chi^3}{15} \end{aligned} \quad (3.64)$$

and

$$\begin{aligned} \chi h_1 &= \frac{\chi^2}{3} - \frac{\chi^4}{30} - \frac{i}{\chi} - \frac{i\chi}{2} \\ [\chi h_1]' &= \frac{2\chi}{3} - \frac{2\chi^3}{15} + \frac{i}{\chi^2} - \frac{i}{2} . \end{aligned} \quad (3.65)$$

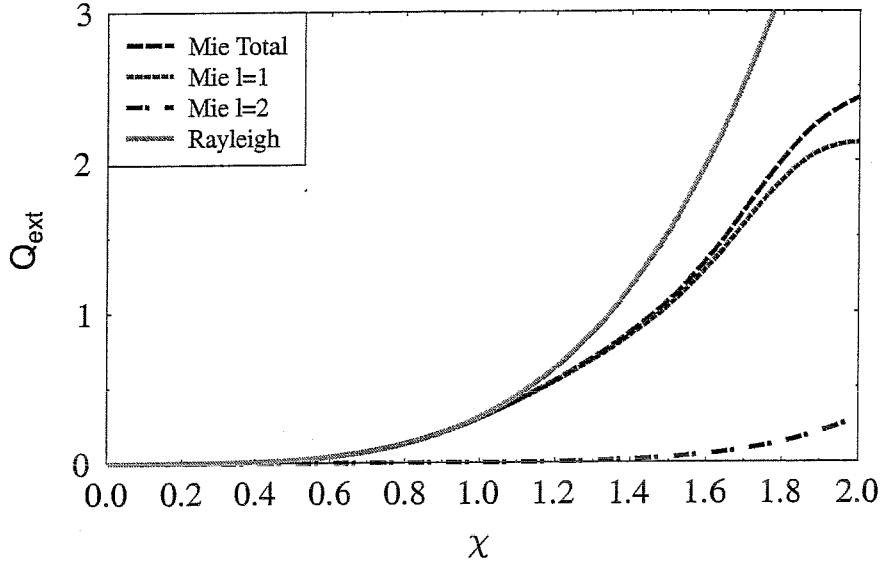


Figure 3.16: Contribution from the two lowest pole orders to the extinction cross section in the Rayleigh regime.

By inserting Equation(3.65) into the expression for Mie scattering coefficients results in

$$\begin{aligned} a_1 &= \frac{4\chi^6}{9} \left( \frac{N^2 - 1}{N^2 + 1} \right)^2 - \frac{i2\chi^3}{3} \left( \frac{N^2 - 1}{N^2 + 2} \right) \\ &\quad - \frac{i2\chi^5}{5} \frac{(N^2 - 2)(N^2 - 1)}{(N^2 + 2)^2} + \dots \end{aligned} \quad (3.66)$$

$$b_1 = \frac{-i\chi^5}{45} (N^2 - 1) + \dots \quad (3.67)$$

where  $N = N_s/N_m$  as before. Substituting these into Equations(3.55) and (3.56) leads to the well known Rayleigh cross sections formula [55] [57]:

$$\begin{aligned} C_{scat} &= \frac{6\pi}{k_m^2} \left[ \frac{4\chi^6}{9} \left| \frac{N^2 - 1}{N^2 + 2} \right|^2 \right] \\ &= \frac{k_m^4}{6\pi} |\alpha|^2 \end{aligned} \quad (3.68)$$

and

$$\begin{aligned} C_{ext} &= \frac{6\pi}{k_m^2} \text{Im} \left[ \frac{-i2\chi^3}{3} \frac{N^2 - 1}{N^2 + 2} \right] \\ &= k_m \alpha'' \end{aligned} \quad (3.69)$$

where  $\alpha = \alpha' + i\alpha''$  is the complex polarizability of a Rayleigh sphere defined by [57]

$$\alpha = 3V \frac{N^2 - 1}{N^2 + 2} \quad (3.70)$$

where  $V$  is the volume of the particle. Equations(3.68) and (3.69) represent expressions of cross sections for the Rayleigh approximation which are used later in Chapter 4 for the determination of optical forces on Rayleigh particles in the evanescent region of a waveguide.

### 3.8.2 Validity of the Rayleigh model

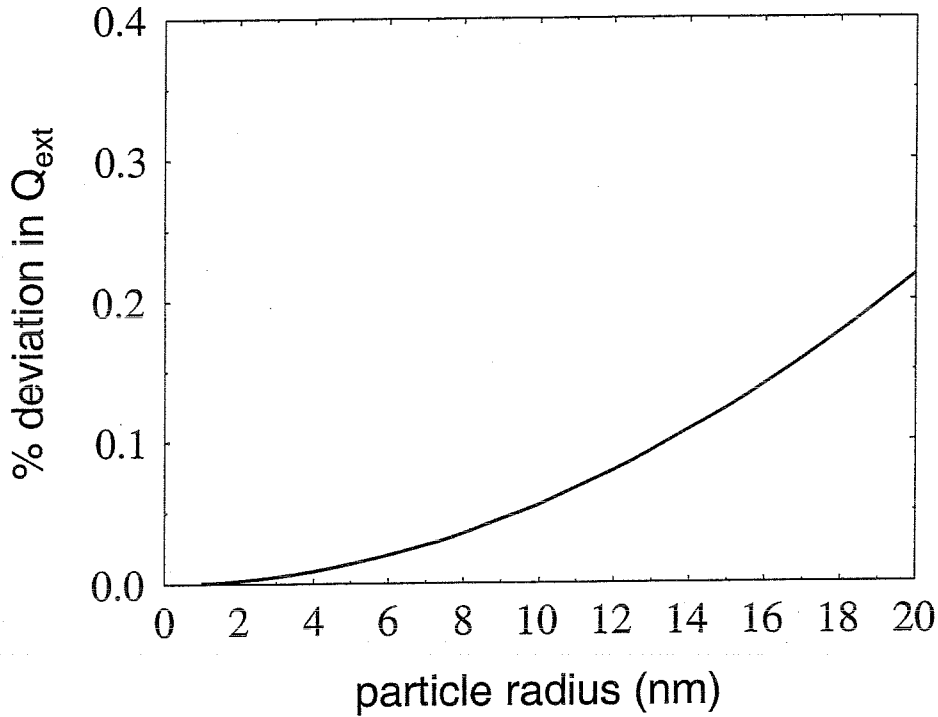


Figure 3.17: Validity of Rayleigh approximation for a latex particle  $N_s = 1.59$  against particle radius in air,  $\lambda = 1\mu\text{m}$ .

Although the Rayleigh approximation serves as a simplification from the more complicated Mie model, its validity needs to be assessed carefully in order to obtain an accurate physical picture of cross sections, fields and intensity distribution around a particle. For this reason, the limiting particle radius satisfying the Rayleigh approximation is evaluated at the point where it starts to deviate. The percentage of deviation is defined here as the variation in  $Q_{ext}$  of the Mie model compared to the Rayleigh model, expressed in a percentage form. For comparison, the validity of the Rayleigh model is evaluated on latex, gold and silver particles as shown in Figure 3.17, Figure 3.18 and Figure 3.19 respectively.

In the case of a lossless latex sphere with an index of  $N_s = 1.59$  at  $\lambda = 1\mu\text{m}$  as shown in Figure 3.17, the deviation of the Rayleigh model from the Mie model is relatively small over the size range considered. For instance, the deviation for a particle radius of  $a = 10\text{nm}$  is less than 0.1%. Hence, the Rayleigh approximation is valid for a lossless latex particle for up to a radius of  $a < \lambda/10$  with a maximum deviation of  $\approx 5\%$  corresponding to  $\lambda = 1\mu\text{m}$ . In addition, the discrepancy between both theoretical models increases as the particle radius increases. Let us explain from the point of view of a Mie particle. For a small radius, a particle can be represented solely by the lowest pole order in which case the polarizability of a particle is valid. However, due to a variation in pole strength and orientation which increases as a particle radius increases, the polarizability of

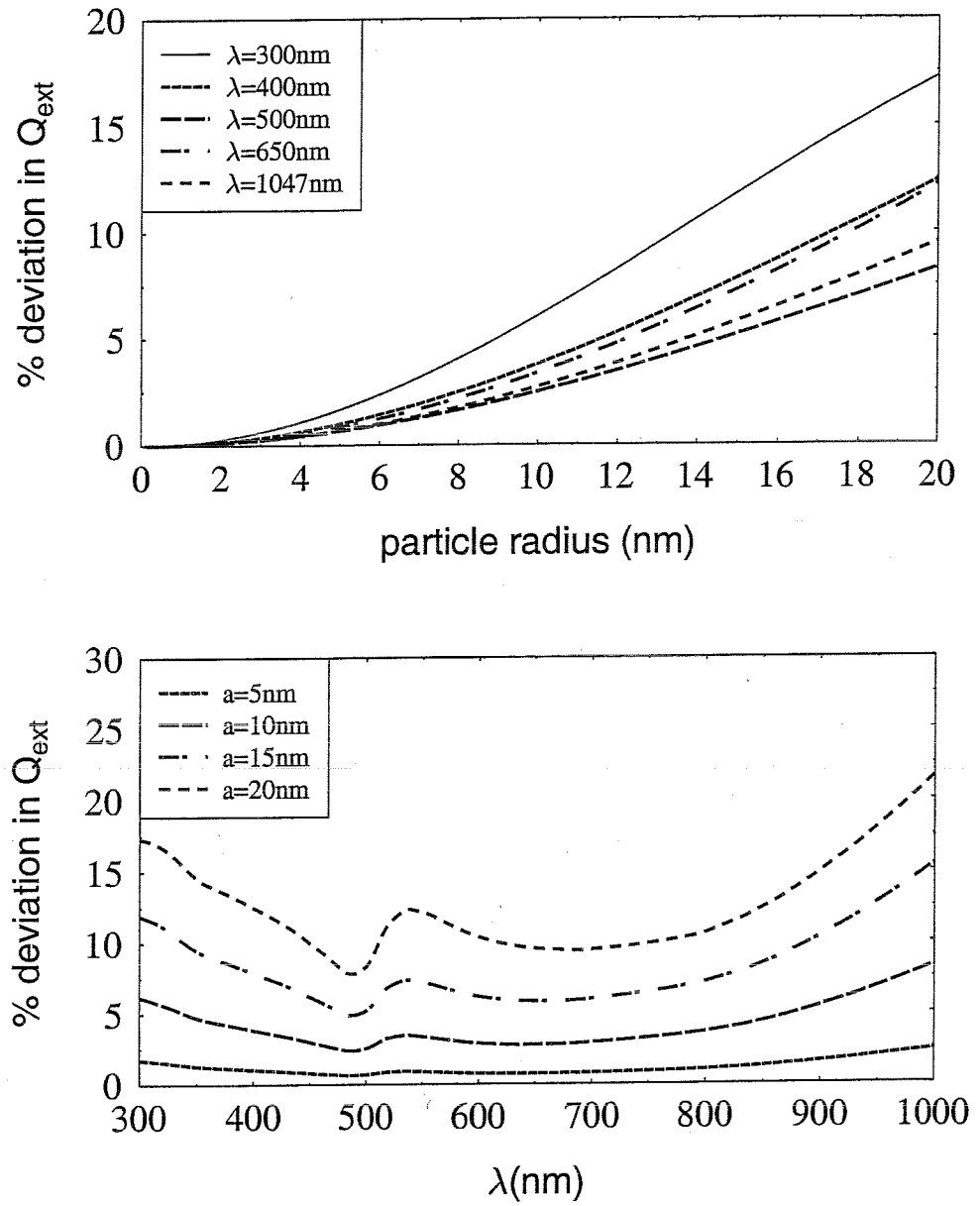


Figure 3.18: Variation of the validity of the Rayleigh model for a gold particle in air, (a) with particle radius and (b) with wavelength.

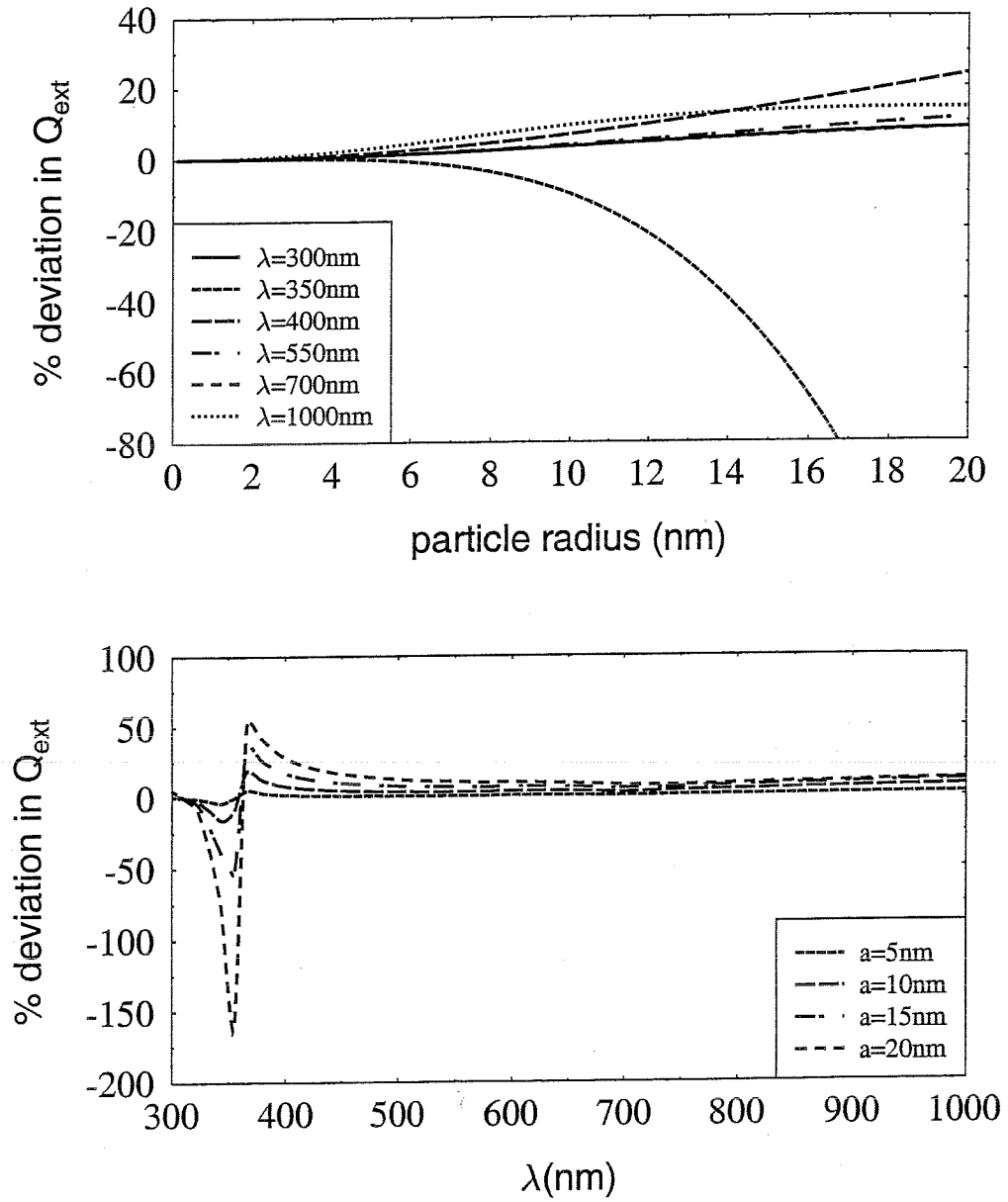


Figure 3.19: Variation of the validity of the Rayleigh model for a silver particle in air, (a)with particle radius and (b)with wavelength.

a particle becomes increasingly invalid. When this occurs, the discrepancy between the Mie and Rayleigh models becomes increasingly critical. Hence, in a way, the deviation as shown is in fact a reflection of the range of validity of the polarizability of a particle.

In Figure 3.18(a), as the radius of a Rayleigh gold particle increases, it approaches a Mie particle which explains the increase in deviation between the two models. As an example, at a wavelength of  $\lambda = 1.047\mu\text{m}$ , the deviation increases from 9.5% for a sphere of 10nm in radius to a deviation of 25% for the same particle but with a larger radius of 20nm. In subsequent chapters and in experiments, due to the small deviation of the Rayleigh  $a = 10\text{nm}$  gold sphere from the Mie theory found here, all calculations based on these particles are carried out using the Rayleigh approximation. Furthermore, in order to illustrate the wavelength dependence of the validity of the Rayleigh range, Figure 3.18(b) clearly shows that at short wavelengths, these particles exhibit a large deviation which decreases with wavelength up to about  $\lambda = 500\text{nm}$ , after which it increases to a peak, corresponding to the plasmon resonance of gold at around 550nm. Note that the characteristics of such a particle defined by its optical properties plays an important role in the validity of the Rayleigh approximation. Unlike a lossless latex sphere, complexity increases in metals where the wavelength-dependent optical constants must not be neglected. In the same way, the percentage variation of the  $Q_{ext}$  of a Rayleigh

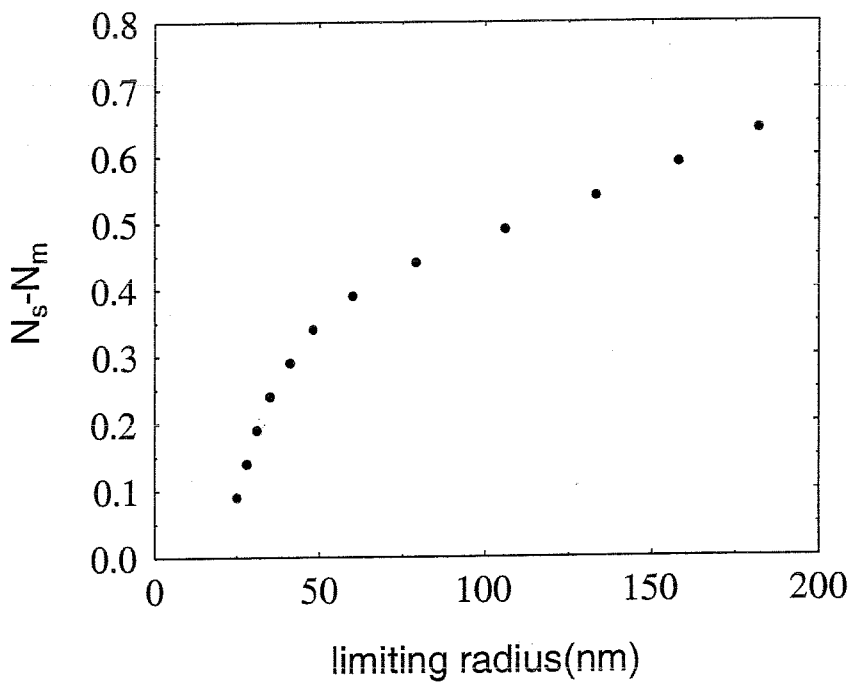


Figure 3.20: Validity of Rayleigh approximation to a deviation of 2% for a latex sphere in a range of surrounding media.

silver sphere in Figure 3.19 shows an increase in the deviation with particle radius. By comparison, a silver sphere of radius  $a = 10\text{nm}$  and  $a = 20\text{nm}$  at  $\lambda = 1.047\mu\text{m}$  results in a percentage deviation of 8% and 17% respectively, in reasonable agreement with a gold sphere. Again, at the wavelength where the silver undergoes plasmon resonances at around  $\lambda = 400\text{nm}$ , the deviation becomes large.

By comparing the deviations found in gold and silver at respective plasmon resonant condition shows that gold exhibits a deviation of  $\approx 3\%$  at  $\lambda = 550\text{nm}$  whereas the deviation for silver is higher at  $\approx 20\%$  at  $\lambda = 400\text{nm}$ . The large difference can partly be explained by the fact that the permittivity of silver particles exhibit a smaller imaginary component  $\epsilon''$  and a real part closer to the condition of  $\epsilon' = -2\epsilon_m$  hence leading to a bigger polarizability and a sharper resonance peak.

In addition, considering a percentage difference of 2%, the effect of increasing the index difference of the particle with respect to the surrounding medium is shown in Figure 3.20 for a latex particle. An increase in particle radius with index difference is analogous to that of the relation between an increase in waveguide effective index and the normalised waveguide thickness. In the case where the index of the sphere becomes increasingly larger than that of the surrounding medium, light is increasingly confined in the particle resulting in larger Rayleigh radius to satisfy the applicability of the Rayleigh model at a 2% deviation.

### 3.8.3 An electrostatic approximation

When particles are small compared to the wavelength, an induced dipole is created as a result of a separation of charges. The relationship between a Rayleigh sphere and an electrostatic approximation is discussed in this section.

Consider a homogeneous, isotropic sphere illuminated by parallel beam in an uniform static electric field where  $\vec{E}_0 = E_0 \hat{z}$ . Due to the discontinuity present at the boundary between the field and sphere which have different permittivity, the initial incident field is altered. The fields inside and outside the sphere,  $\vec{E}_s$  and  $\vec{E}_m$  respectively can be related to the scalar potentials by

$$\vec{E}_s = -\nabla V_s \quad (r < a), \quad \vec{E}_m = -\nabla V_m \quad (r > a) \quad (3.71)$$

hence, at the boundary where  $r = a$ , the potentials must satisfy

$$\vec{V}_s = \vec{V}_m \quad \epsilon \frac{\partial \vec{V}_s}{\partial r} = \epsilon_m \frac{\partial \vec{V}_m}{\partial r} \quad (3.72)$$

Also, we have to assume that at large distance, the electric field represents the unperturbed applied field, hence,

$$\lim_{r \rightarrow \infty} \vec{V}_m = -E_0 r \cos\theta = -E_0 z \quad (3.73)$$

By solving the boundary conditions using Equations(3.72) and (3.73), one can arrive at the field inside and outside the sphere, which for  $r < a$  is given as

$$\vec{E}_s = \frac{3\epsilon_m}{\epsilon + 2\epsilon_m} E_0 r \cos\theta \quad (3.74)$$

and for  $r > a$

$$\vec{E}_m = -E_0 r \cos\theta + a^3 E_0 \frac{N^2 - 1}{N^2 + 2} \frac{\cos\theta}{r^2} \quad (3.75)$$

It is interesting to note that the field outside the sphere,  $\vec{E}_m$  consists of two components; The first term is the applied field  $\vec{E}_0$ , and superimposed upon it is the second term which is identical to an

induced field characteristic of a dipole [54] [55]. The dipole moment is written as [55]

$$\vec{p} = 4\pi\epsilon_0\epsilon_m a^3 \frac{N^2 - 1}{N^2 + 2} \vec{E}_0 \quad (3.76)$$

and is commonly expressed as  $\vec{p} = \epsilon_0\epsilon_m\alpha\vec{E}_0$  [57]. This clearly explains the origin of the polarizability of a material  $\alpha$ . By a comparison with Equations(3.68) and (3.69) and applying Equation(3.70) results in a similarity which suggests an equivalence of a Rayleigh particle and a dipole scatter.

### 3.9 Intensity distribution around a Mie dielectric sphere

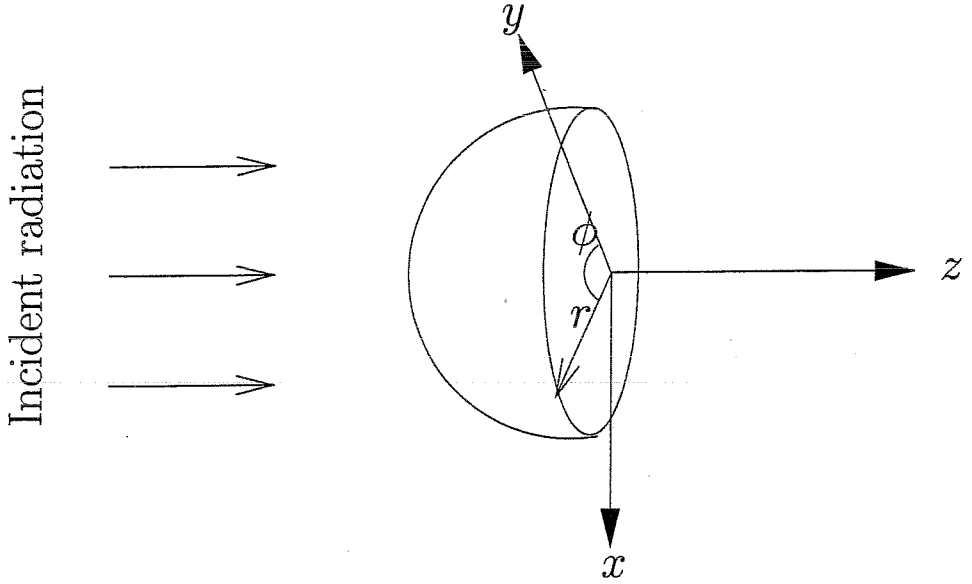


Figure 3.21: Cross section of a sphere illuminated by a plane wave.

Based on Equation(3.37), and using Equations(3.45) and (3.43), the incident, scattered and internal electric fields for a plane wave incidence are [55]

$$\vec{E}_{inc} = E_0 \sum_{l=1}^{\infty} i^l \frac{(2l+1)}{l(l+1)} [\vec{M}_{l,1,o} - i\vec{N}_{l,1,e}] \quad (3.77)$$

$$\vec{E}_{scat} = -E_0 \sum_{l=1}^{\infty} i^l \frac{(2l+1)}{l(l+1)} [b_l \vec{M}_{l,1,e} - ia_l \vec{N}_{l,1,o}] \quad (3.78)$$

and

$$\vec{E}_{int} = E_0 \sum_{l=1}^{\infty} i^l \frac{(2l+1)}{l(l+1)} [c_l \vec{M}_{l,1,o} - id_l \vec{N}_{l,1,e}] \quad (3.79)$$

Note that only components of  $\vec{M}_{l,1,o}$  and  $\vec{N}_{l,1,e}$  exist due to the fact that  $\Pi_{l,m}$  vanishes for even  $l$  while  $T_{l,m}$  vanishes for odd  $l$ . Corresponding magnetic fields can be similarly obtained by using the relations in Equation(3.3). Distribution of the scattered and internal intensities which are discussed

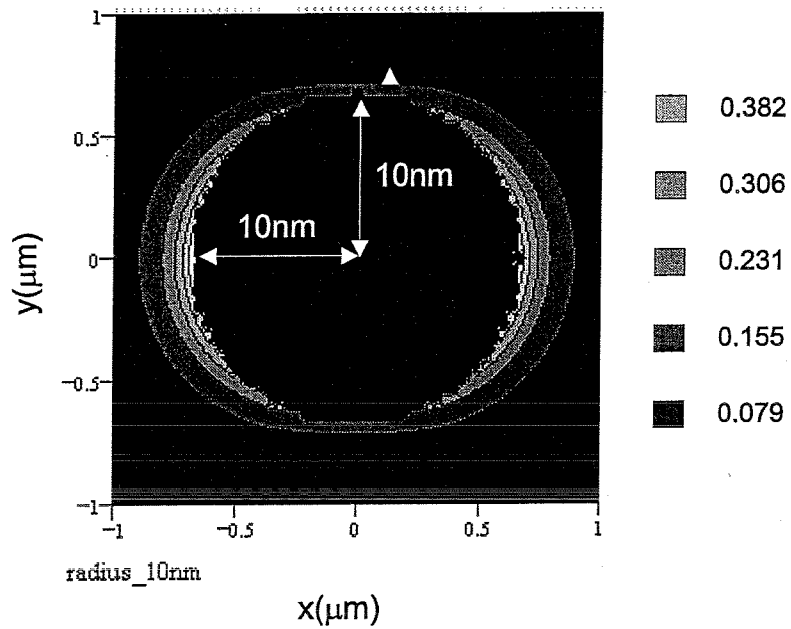


Figure 3.22: Contour plot of intensity distribution for a latex sphere of  $a = 10\text{nm}$  in air,  $\lambda = 1\mu\text{m}$ . A scanning resolution of  $\Delta x = \Delta y = 0.5 \times \text{nm}$  is assumed.

next, are determined from the proportional relationship between intensity and field amplitude where  $I \propto |\sqrt{E_r^2 + E_\theta^2 + E_\phi^2}|^2$ . A size parameter resolution of  $\Delta \chi = 10^{-3}$  was used throughout the analysis.

Under the influence of an incident beam, light is emitted from a particle resulting in a scattering pattern at a distance larger than the particle radius, ie:  $r > a$ , and an internal intensity pattern for distances smaller than the particle radius, ie:  $r < a$ . As a particle increases, more modes may be excited by the partial wave coefficients as described in Section 3.7.2 depending on  $\chi$ , hence leading to a different internal and scattering intensity pattern. The study of the scattering and internal intensity distribution around a Rayleigh sphere and a comparison to a Mie sphere will be described in this section. As before, the same parameters are used where a latex particle with an index of  $N_s = 1.59$  and  $K = 0$  with air as the surrounding medium is considered. The results obtained would be useful for predicting signal enhancement of a tagged Raman molecule attached to the particle surface, for example.

The geometry of the cross section considered is shown in Figure 3.21. In all cases, a plane wave is assumed to propagate along the  $z$ -axis with an incident angle of  $\theta = 0^\circ$ . As indicated in Figure 3.21, the cross section under consideration lies in the  $x - y$  plane with an azimuthal angle  $\phi$  ranging from  $0^\circ$  to  $360^\circ$  and, an imaginary radius from  $r = 0$  to  $r = R_1$  where  $R_1 > a$ . Based on Equations(3.78) and (3.79), the distribution of the intensity is illustrated in Figure 3.22 for a Rayleigh sphere with  $a = 10\text{nm}$ , and in Figure 3.23 for a Mie latex sphere with  $a = 3\mu\text{m}$ , where the corresponding size parameters are  $\chi = 0.068$  and  $\chi = 18.85$  respectively. In all cases, the particle is centered at the origin of each plot shown below. The legend beside each plot indicates the magnitude of the intensity expressed in  $\text{V}^2/\text{m}^2$ .

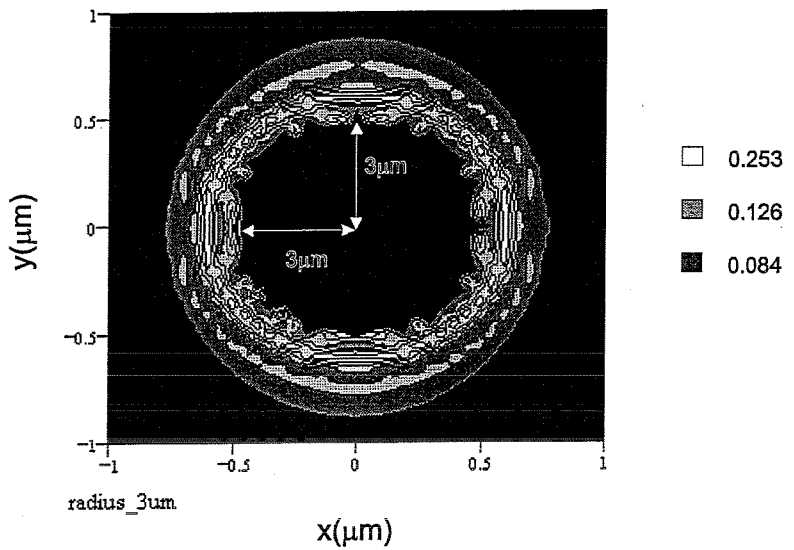


Figure 3.23: Contour plot of intensity distribution on a latex sphere of  $a = 3\mu\text{m}$  in air,  $\chi = 18.85$ . A scanning resolution of  $\Delta x = \Delta y = 0.05\mu\text{m}$  is assumed.

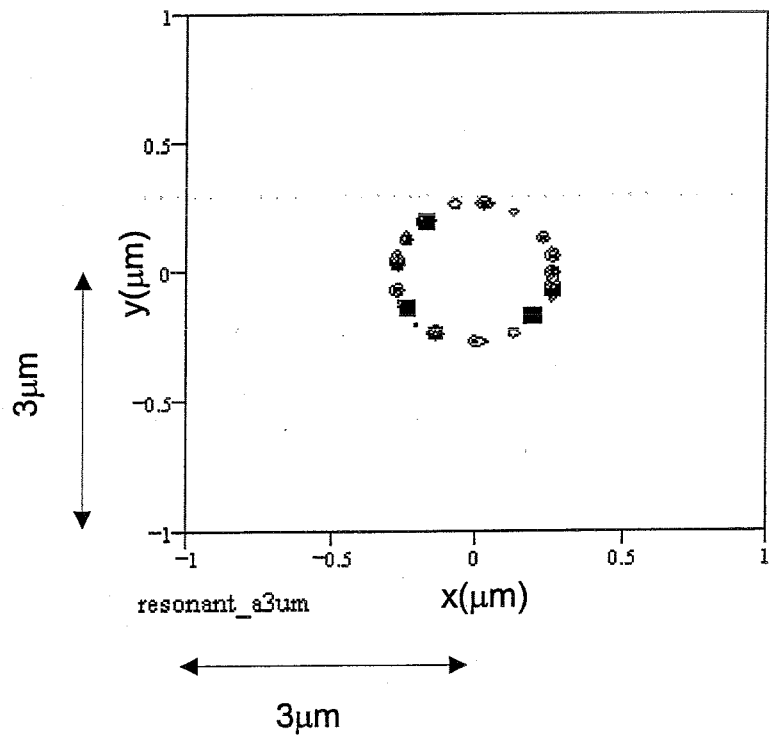


Figure 3.24: Contour plot of intensity distribution with a larger scanning resolution of  $\Delta x = \Delta y = 0.1\mu\text{m}$  for the same set of parameters considered in Figure 3.23. The resonant modes corresponds to an intensity of  $8.76 \times 10^6 \text{V}^2/\text{m}^2$ .

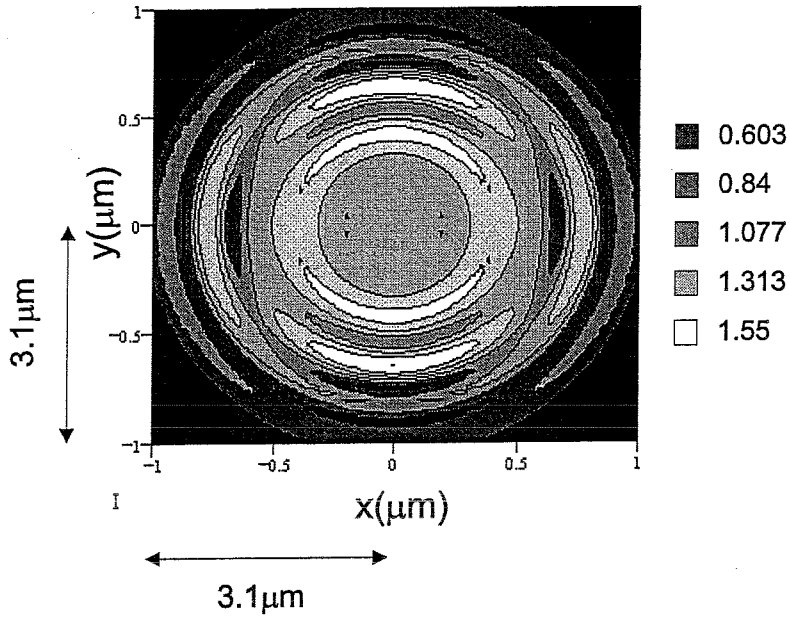


Figure 3.25: Contour plot of intensity distribution for a non-resonant condition on a latex particle with a radius of  $a = 3.03\mu\text{m}$  in air,  $\chi = 19$ . The scanning resolution is the same as considered in Figure 3.24.

As a Rayleigh sphere can be treated as a dipole, the intensity within the particle acted upon by a homogeneous field is constant, in agreement with Figure 3.22 for  $r < a$ . However, for  $r > a$ , the intensity is observed to decay with increasing distance away from the Rayleigh sphere. In contrast, the intensity pattern of a Mie particle as shown in Figure 3.23 and Figure 3.24 where the scanning resolution in the latter case is 10 times larger than the former, reveals a distribution of highly localised intensity regions around the particle for  $r < a$ . The reason for an absence of scattered intensity in Figure 3.24 is due to the large magnitude difference compared to the resonant intensity.

Based on Figure 3.9 and Figures 3.12-3.13, a resonant feature originating from  $b_{25}^1$  and  $c_{25}^1$  with a pole order of 25, is generated on a latex particle with a radius of  $a = 3\mu\text{m}$  and a corresponding size parameter of  $\chi = 18.85$ . The fact that 17 instead of 25 highly intense regions is found in Figure 3.24 suggest an even higher scanning resolution required for achieving a greater accuracy. This has not been pursued due to a limitation in computer memory space.

In Figure 3.25, an example is given to illustrate the intensity distributed around a particle off resonance. In this case, a latex sphere with a particle radius of  $a = 3.03\mu\text{m}$  and a corresponding size parameter of  $\chi = 19$ , which does not contribute to a resonance based on Figure 3.9, is considered. By a comparison of both the resonant and non-resonant cases in Figure 3.24 and Figure 3.25 respectively, morphology-dependent resonance in the particle is clearly demonstrated.

Note that the intensity distribution in the equatorial geometry as reported by Reference [51] indicates a stronger forward intensity at  $\theta = 0^\circ$  compared to a relatively weak backward intensity, analogous to the case of a focusing lens. Besides, the origin of the behaviour can be traced back to the angular distribution of the associated Legendre polynomials in  $\Pi_{l,m}$  and  $T_{l,m}$  based on Figures

3.2-3.5, where the forward lobe is enhanced whilst the backward lobe at  $\theta = 180^\circ$  is reduced with increasing number of poles  $l$  for a large sphere.

### 3.10 Evanescent wave excitation

Having established a good understanding of the physical picture underlying particle-light interaction in the general plane wave case, the behaviour of a particle based on an excitation of an evanescent wave is investigated next. A schematic of this problem has been shown in Figure 2.1 of Chapter 2. However, in this case a simple infinite slab with an index of  $n_g = 1.5$  and a latex particle is located at the surface with air as the surrounding medium. The purpose of choosing this configuration is so that it can be compared to the general plane wave case previously considered.

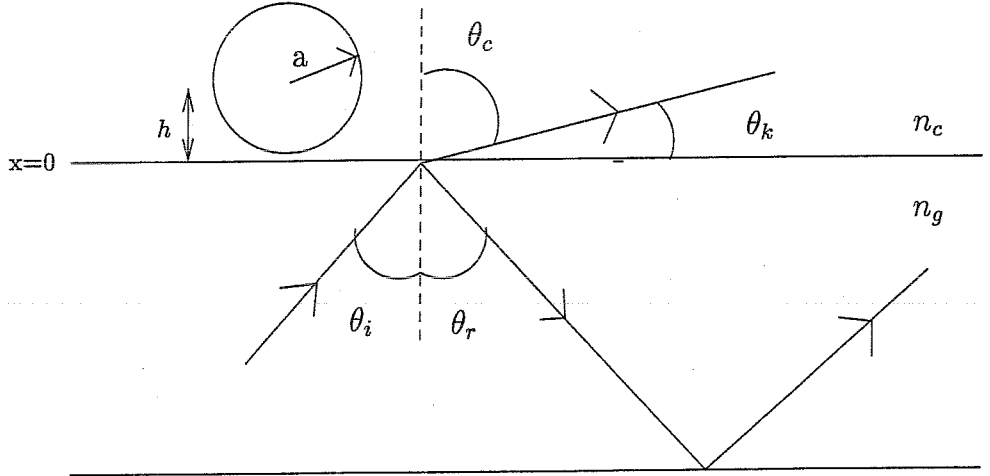


Figure 3.26: Total internal reflection by an incident plane wave in an optically dense medium. A small perturbation in the cover region results in a decaying evanescent wave.

Based on Figure 3.26 and by Snell's law where  $n_g \sin \theta_i = n_c \sin \theta_c$ , when light is incident at the critical angle denoted by  $\theta_{crit}$ , a plane wave results which travels along the surface of the waveguide. As  $\theta_i$  increases above the critical condition, light becomes totally internally reflected and the confinement of light in the guiding region forms a waveguide. Under total internal reflection, a damped wave characterised by a decaying magnitude away from the surface propagates in the cover region. Due to its rapid decay, this is commonly termed an evanescent wave. Under such conditions, the refracted angle into the cover region is complex. More specifically,  $\cos \theta_k < 1$  and  $\sin \theta_k$  becomes purely imaginary. Hence, unlike the case of a plane wave, an evanescent wave results in angular terms of  $\Pi_{l,m}, T_{l,m} \geq 1$  which must be taken into account in the expressions for cross sections, for instance.

Assuming that both the particle and the cover medium are isotropic, homogeneous, nonmagnetic and nonconducting with permittivities  $\epsilon = \epsilon' + i\epsilon''$  and  $\epsilon_m$  respectively, a discontinuity is present when the incident beam traverses the particle. Consequently, light is extinguished in the form of scattering and absorption. Since the effect of multiple reflections between the particle and the

boundary upon the incident field is found to be insignificant and can be neglected for particle radius  $a < 30\mu\text{m}$  [50], it is not taken into consideration in this analysis.

From the discussion in Chapter 2, a particle is assumed to interact with maximum surface irradiance and intensity gradient at the guide-cover interface where the centre of the particle is at a distance of  $h = a$  from the surface. In this case, the strongest resonant effect is expected [60]. A final point to note concerns the depth of an evanescent wave which is typically in the order of hundreds of nanometer. This means that in order for an appreciable force to act on the whole sphere, it has to lie well within this regime. One way of ensuring this is to create sufficient gradient force which is able to pull a particle onto the higher intensity region of the waveguide surface. In the case of a particle larger than the penetration depth, it has been reported that the bottom surface of the sphere which interacts stronger with the decaying field limited to a penetration depth of  $\approx 500\text{nm}$  for instance, will experience a larger change in momentum resulting in a more significant resonance effect than the upper surface [60].

In the following sections, results comparing the resonance in  $Q_{ext}$  for a particle excited by a plane wave and an evanescent wave will be presented. Comparison will also be given for two different angles of incidence.

### 3.10.1 Extinction spectral of latex spheres

Based on Equations (3.56) and (3.61), Figure 3.27 shows the extinction plots for both TE and TM polarizations. Two incident angles have been chosen where Figures 3.27(b) and (c) correspond to  $\theta_i = 61.81^\circ$  while Figures 3.27(d) and (e) correspond to a larger angle of  $\theta_i = 87.647^\circ$ . The latter results in an evanescent penetration depth typical of a potassium ion-exchanged waveguide with a NA of  $\approx 0.17$ . For comparison, the extinction spectrum for an incident plane wave is also shown in Figure 3.27(a). As an illustration, the spectral range of  $10 < \chi < 15$  is selected. As before, a total number of 40 poles and a resolution of  $\Delta\chi = 10^{-3}$  are used.

Each resulting spectrum in Figures 3.27(a)-(e) illustrates a contribution from partial wave coefficients. Specifically, the resonant feature at size parameters of  $\chi = 12$  and  $\chi = 12.35$  are due to partial wave contributions from  $b_{15}^1$  and  $a_{15}^1$  respectively. Note that the these coefficients are selectively enhanced in the TM and TE spectra where one enhances the smaller peak of the other spectral, in agreement with results in References [44] and [62]. Although both TE and TM resonant modes contribute to the plane wave spectral, an apparent difference lies in the magnitude of  $Q_{ext}$ , where owing to the penetration of a perturbed evanescent wave into the particle allowing a stronger excitation, an enhancement by two orders of magnitude can be generated, in agreement with results found in References [44] and [62].

Besides, a stronger resonance is associated with TM as compared to TE polarization. This can be explained by the larger surface intensity in TM polarization which increases the particle light interaction. By inspection, the resonant structures get sharper and narrower with increasingly enhanced peaks as the size parameter increases corresponding to larger morphology-dependent resonance generated by a larger sphere. Finally, resonances are stronger for a smaller angle of incidence which

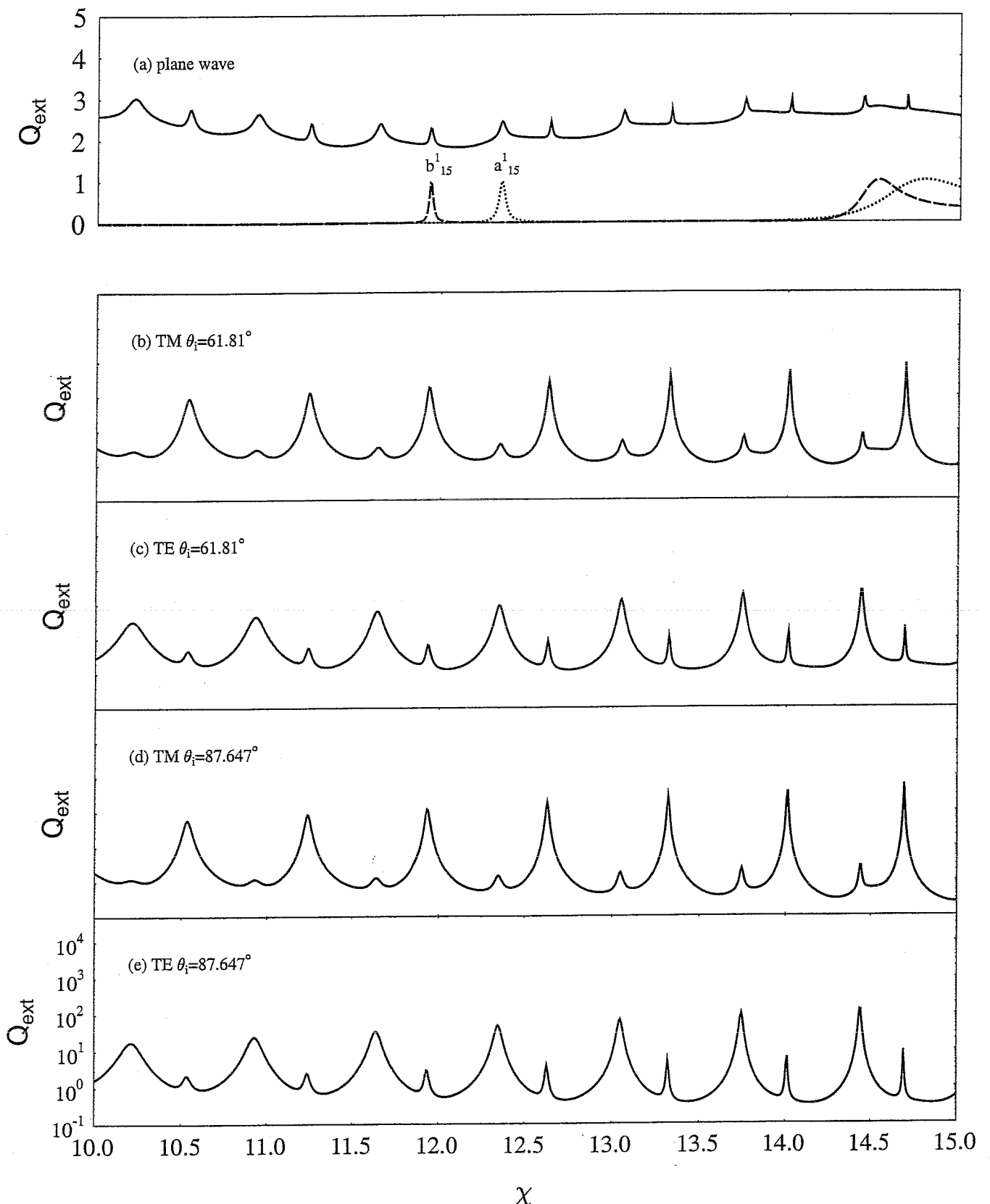


Figure 3.27: Extinction spectral of latex sphere on a waveguide with incident angle of  $61.81^\circ$  in (b),(c),  $87.647^\circ$  in (d),(e), for both TM and TE polarizations. Comparison is made against the plane wave case in (a). The scale for figures (b)-(d) follows that of (e) which represents a log scale.

corresponds to a greater penetration of the evanescent field into the cover region.

### 3.10.2 Extinction spectral of metallic spheres

#### 3.10.2.1 Introduction

The principal difference in optical behaviour between metallic and dielectric particles lies in the strongly wavelength-dependent optical constants of metals. In general, both gold and silver Rayleigh spheres possess a large and negative real part of the permittivity  $\epsilon'$  in the visible region, whose magnitude decreases as the wavelength increases into the infrared region. The imaginary part of the permittivity, on the other hand, increases significantly at large wavelengths. Because of this, plasmon resonance or bulk resonance of these metals, which is due to the excitation of the conduction electrons within a material, are found in the short wavelength region specifically when the condition  $\epsilon' = -2\epsilon_m$  is met.

The aim of this following section is to investigate the extinction spectral for gold and silver particles under evanescent wave excitation. In the first part, the contribution of individual poles to the total extinction spectrum for a range of particle radii will be presented. Next, a comparison between the spectra for both TM(p-pol) and TE(s-pol) polarizations of an evanescent wave with an incident angle of  $87.647^\circ$ , typical of an ion-exchange waveguide as mentioned, is compared against the plane wave case based on Equation(3.60) where  $F_{l,m}, H_{l,m} = 1$ . As shown previously in Figure 3.27, the asymmetrical nature of an evanescent wave enhances the excitation of modes within a particle which may not be realised by a normal plane wave. Consequently, an enhancement in the extinction spectrum is predicted. Finally, the extinction efficiency for both cases will be examined over a range of size parameter to investigate the presence of morphology-dependent resonance.

The behaviour of silver particles is included in the analysis for two reasons. Firstly, both gold and silver particles produce sharp plasmon resonances which are useful in applications such as surface-enhanced Raman spectroscopy(SERS) where these materials can be used as a surface coating around a sensing biological molecule for the detection of Raman signals. Secondly, a direct comparison to Quinten's results in Reference [44] which compare the cross sections obtained by a plane wave and that by an evanescent wave helps to confirm the accuracy of the present model which is later extended to investigate a gold particle.

#### 3.10.2.2 Contribution from individual poles to $Q_{ext}$

In Figure 3.28, the extinction efficiency  $Q_{ext}$  of gold spheres corresponding to four radii of 10, 40, 100 and 250nm is shown in (a)-(d) over a range of wavelength. On each plot, the individual pole contribution is shown. As for the case of latex particle, only the lowest order pole  $l = 1$  contributes significantly to the total spectral for particles with a small radius as shown in Figure 3.28(a) and (b) corresponding to particle radius of  $a = 10\text{nm}$  and  $a = 40\text{nm}$  respectively. In this case, a particle effectively acts as a simple dipole. As the size increases, second and higher order poles become significant which is accompanied by a red-shift of the lower order pole as evidently shown in Figure

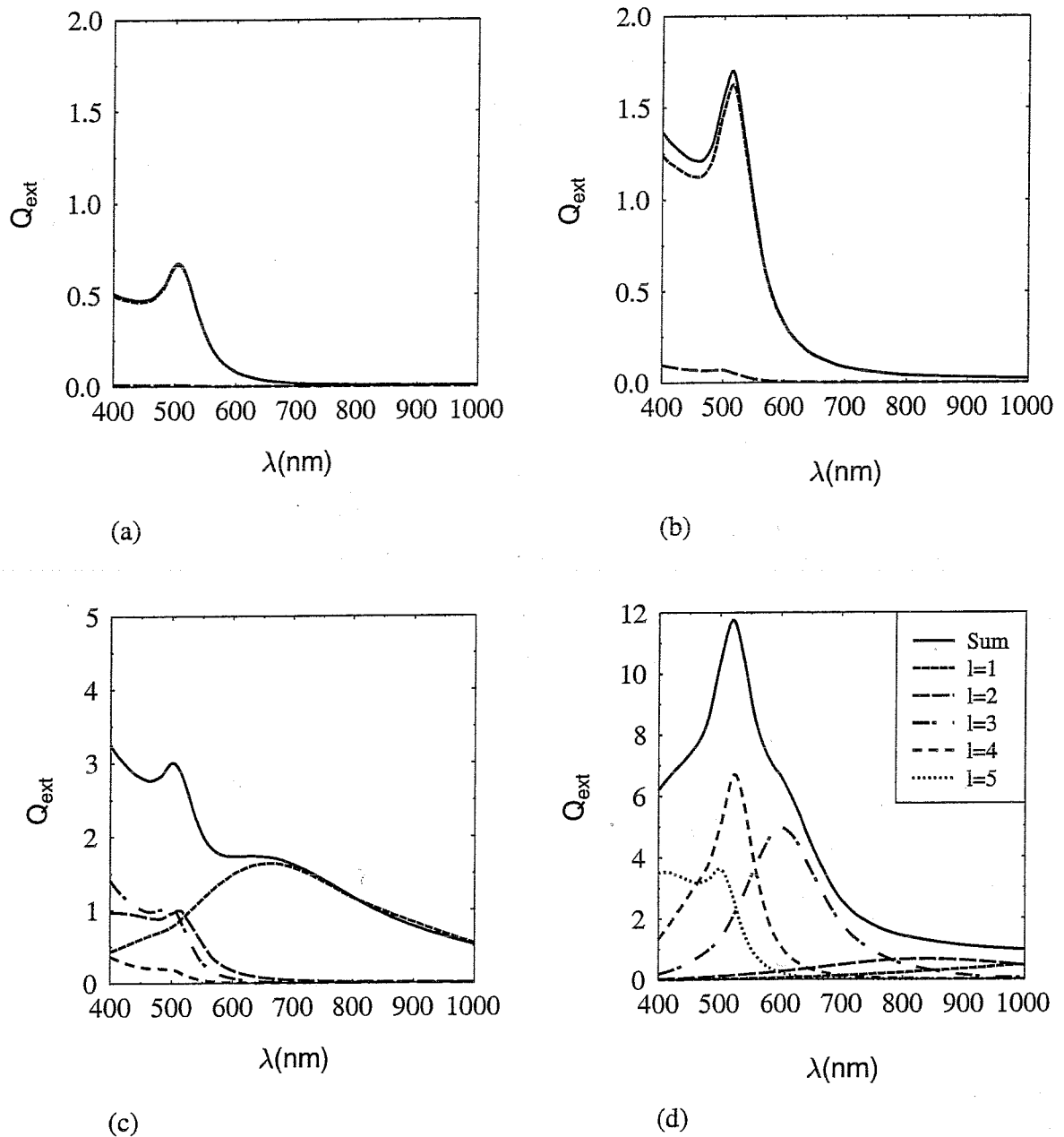


Figure 3.28: The superposition of poles contributing to the extinction spectral of a gold sphere with radius (a) 10 nm, (b) 40 nm (c) 100 nm and (d) 250 nm.

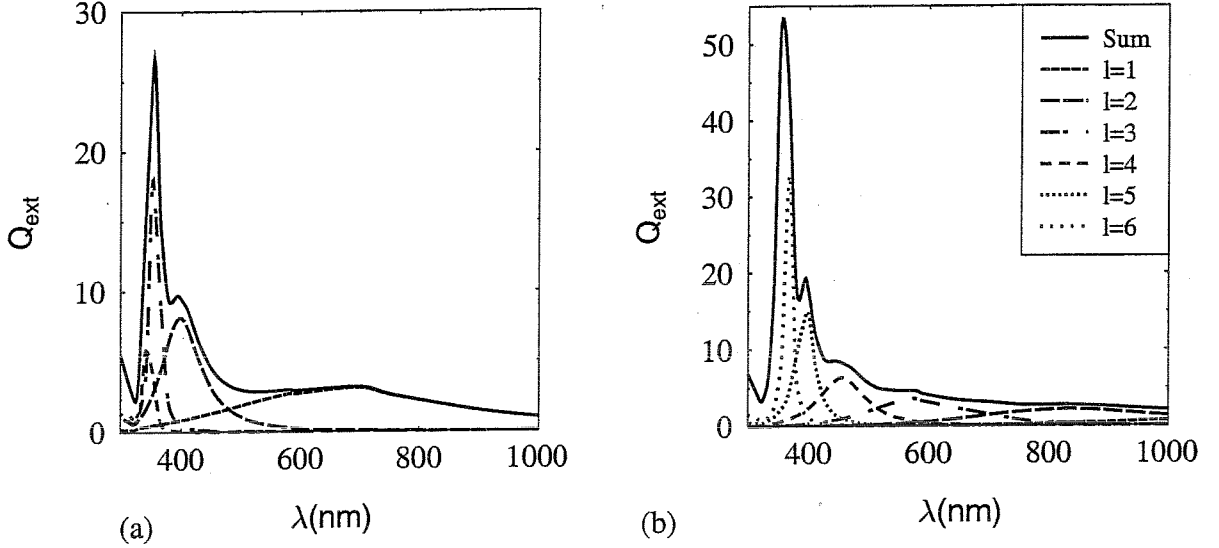


Figure 3.29: The superposition of poles contributing to the extinction spectral of a silver sphere with radius (a) 100nm and (b) 250nm.

3.28(c) for  $a = 100\text{nm}$  and in (d) for  $a = 250\text{nm}$ , for a smaller size parameter  $\chi$ . Specifically, a gold sphere with a particle radius of 100nm clearly exhibits two resonant peaks where, in addition to the plasmon resonance at  $\lambda = 550\text{nm}$  being excited by pole orders of  $l = 2$  and  $l = 3$ , a second peak emerges at a longer wavelength of  $\lambda \approx 650\text{nm}$  due to the red-shifted  $l = 1$  pole component. Strictly speaking, in this case, the particle stops acting as a dipole and the Rayleigh approximation described previously will not be valid.

As a comparison, the extinction spectral with contributions from individual components for silver spheres of radii 100nm and 250nm are shown in Figure 3.29 with optical constants obtained from Reference [65]. The result in Figure 3.29(a) for a particle radius of  $a = 100\text{nm}$  corresponds closely to Quinten's results in Reference [44] in which case two sharp peaks are exhibited at  $\lambda = 380\text{nm}$  and  $\lambda = 400\text{nm}$  whilst a broadened structure is found at a longer wavelength of  $\lambda = 600\text{nm}$ . These peaks correspond to contribution from decreasing pole orders of  $l = 3$ ,  $l = 2$  and  $l = 1$  respectively. By inspection of Figure 3.29(a), the peak at  $\lambda \approx 380\text{nm}$  corresponding to plasmon resonance of silver, is particularly enhanced possibly due to the difference in the set of optical constant data employed for silver particles. By a comparison with a larger particle with a radius of 250nm again emphasizes the red-shifting of the lower pole orders. Note that for the same particle radius of  $a = 100\text{nm}$  for instance, the maximum extinction efficiency of silver is  $\approx 10$  times larger than gold. However, despite the fact that silver exhibits greater enhancement than gold, because it is more prone to chemical reaction than gold which is more inert, the latter is a more favoured candidate for sensing applications.

### 3.10.2.3 The difference in $Q_{ext}$ for evanescent and plane wave excitation

In Figure 3.30 and Figure 3.31, the extinction efficiency spectra for both gold and silver particles in air, are illustrated for the three cases of plane wave, TM(p-pol) and TE(s-pol) evanescent wave excitation considering the same geometry as for a latex particle in Section 3.10.1. For a Rayleigh gold and latex particle with a radius of  $a < 100\text{nm}$ , results depicted in Figure 3.30(a), (b) and Figure 3.31(a), (b) show that the plane wave extinction spectral lies between that of the TM and TE spectral of the evanescent case where the former exhibits a larger magnitude. This further stresses the fact that for a sufficiently small particle, the field around it is virtually homogeneous and uniform approximating that of a plane wave. As the particle size increases, ie:  $> 100\text{nm}$ , note from both sets of plots that the extinction efficiency corresponding to a plane wave excitation is severely damped which results in the smoothing out of resonant peaks, particularly evident in both cases corresponding to a radius of  $250\text{nm}$  and  $500\text{nm}$ . In contrast, resonant peaks remain strongly enhanced for the evanescent case, particularly for TM polarised light which has a larger surface irradiance at the guide-cover interface of a waveguide. Finally, by comparison of the results shown in Figure 3.31(c) with that of Reference [44] for a silver particle of a radius  $a = 100\text{nm}$  shows a good agreement for the plane wave case, although a more enhanced peak was found in our results for the TE(p-pol) evanescent wave excitation at  $\lambda \approx 380\text{nm}$ , possibly due to a different set of optical constants for silver particles employed in this case.

### 3.10.2.4 Variation of $Q_{ext}$ with $\chi$

The variation of the extinction efficiency with size parameter is shown in Figure 3.32 and Figure 3.33 for gold and silver particles respectively. A few interesting points are highlighted as follows:

1. By a comparison to the case of a latex particle as shown in Figure 3.7, it is apparent that resonance of the metallic spheres in the Mie regime is largely damped for  $\chi > 10$  [51].
2. A ripple structure, which is more pronounced for a silver particle, is present thus suggesting the emergence of morphology-dependent resonance peaks as  $\chi$  increases.
3. The ripples are sharpest near the plasmon resonance wavelength of the particle.
4. The extinction efficiency of gold and silver particles is a strong function of wavelength due to their strongly wavelength-dependent polarizability.

## 3.11 Discussion and conclusion

An overview of the Mie theory has been presented which provides a detailed description of the interaction of light with spherical particles. In particular, the origin of morphology dependent resonance(MDR) has been studied and expressions of cross sections and efficiency factor has been studied considering both the evanescent wave and the simplified case of a general plane wave.

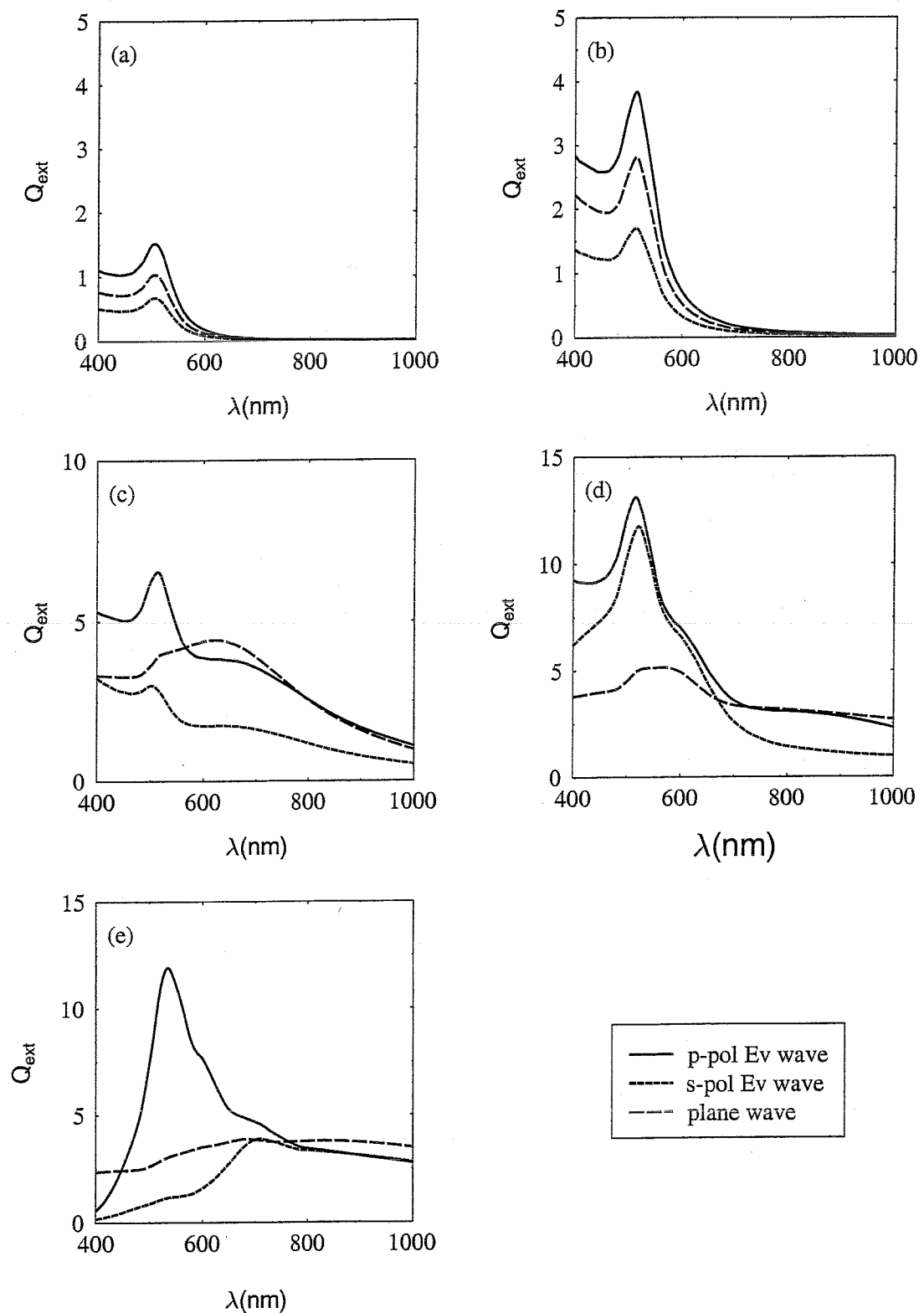


Figure 3.30: Gold spheres: A comparison of an evanescent wave extinction for both TM(p-pol) and TE(s-pol) polarizations, and plane wave excitation for a range of particle radius (a)10nm, (b)40nm, (c)100nm, (d)250nm and (e)500nm.

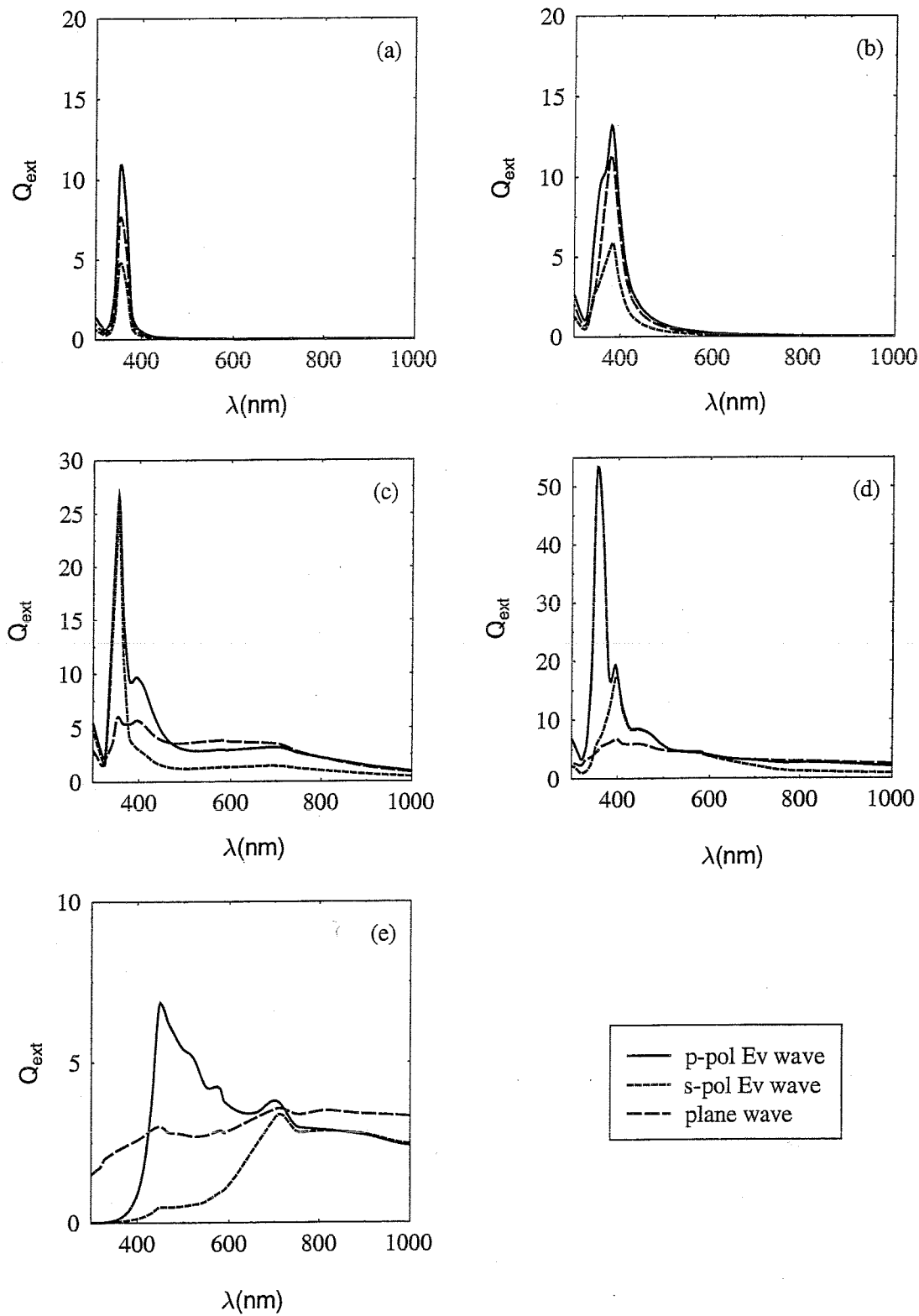


Figure 3.31: Silver spheres: A comparison of an evanescent wave extinction for both TM(p-pol) and TE(s-pol) polarizations, and plane wave excitation for a range of particle radius (a)10nm, (b)40nm, (c)100nm, (d)250nm and (e)500nm.

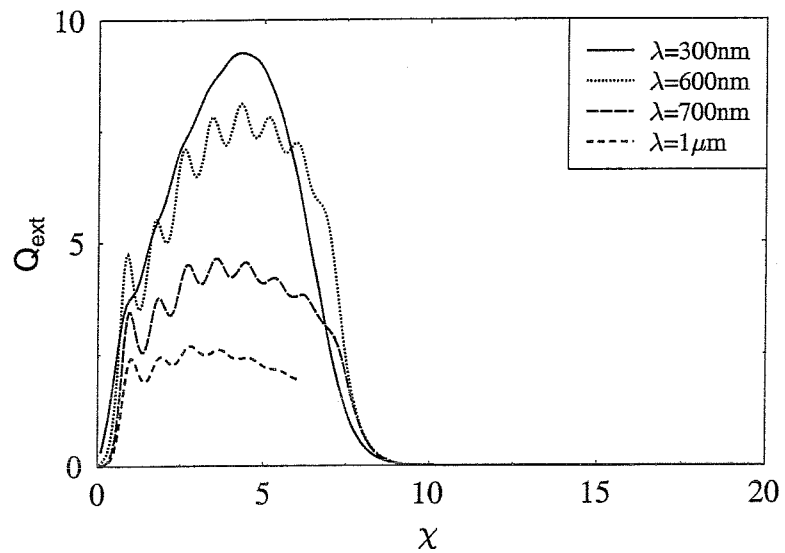


Figure 3.32: Extinction spectral of gold particles versus size parameter for a range of wavelengths.

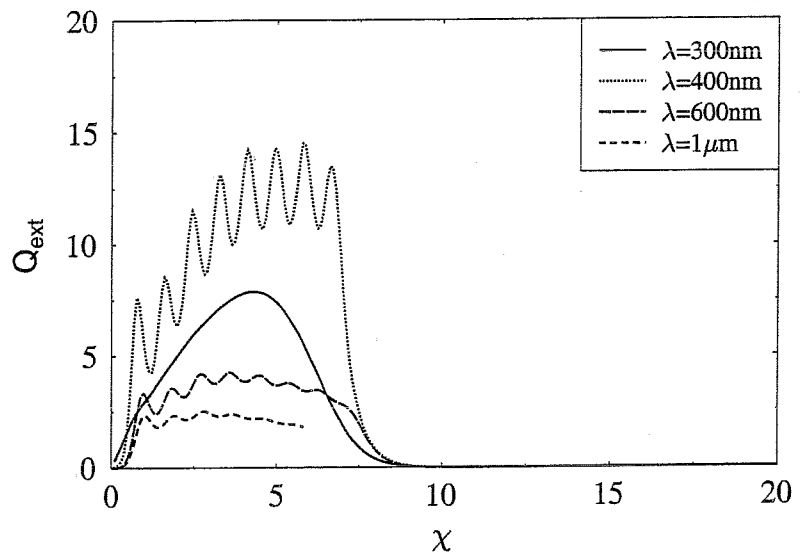


Figure 3.33: Extinction spectral of silver particles versus size parameter for a range of wavelengths.

An important highlight of the results is the evidence of sharp morphology-dependent resonances in latex spheres for particle radius  $a > \lambda$ . These resonances was found to be further enhanced in the evanescent case where asymmetry leads to a stronger effect. Apart from a large particle size, MDR in a dielectric sphere was found to increase with a small imaginary part of index component and maximum index difference between the particle and its surrounding medium. With larger particles, superposition of multiple reflections within the sphere leads to enhanced modes. Besides, a smaller imaginary index and stronger index difference results in a more highly confined radiation in the particle thereby enhancing the effect of the resonant structure.

In contrast, a small Rayleigh sphere obeys the electrostatic approximation where the only contribution to the total extinction and cross section spectra lies in the lowest pole order of  $l = 1$ . Hence, Rayleigh sphere can be treated as equivalent to a simple dipole. For this special case, simplification of the Mie theory allows derivation of simple expressions of cross sections and efficiency factor from which the polarizability of a particle which relates to optical forces as described later in Chapter 4 can be obtained. Results were also presented for the first time on the validity of the Rayleigh approximation obtained by a comparison with the Mie model applying to latex, gold and silver particles. For a particle radius of 10nm at  $\lambda = 1\mu\text{m}$ , the corresponding percentage deviations are 0.3%, 10% and 8% for latex, gold and silver particles respectively. Since the deviation for a gold and a latex particle of this radius are relatively small, the Rayleigh approximation will be used in the derivation of forces as discussed later in Chapter 4.

Unlike dielectrics, metallic spheres exhibit plasmon resonances in the visible region, ie:  $\lambda \approx 550\text{nm}$  for gold and and  $\lambda \approx 380\text{nm}$  for silver. These are manifested in the  $Q_{ext}$  spectral which shows a narrow peak at this wavelength corresponding to the condition where the particle has the largest  $\epsilon'$  close to  $-2\epsilon_m$  and a small imaginary component. The main difference between the results obtained for metallic spheres compared to dielectrics is that unlike the case of a latex particle, the  $Q_{ext}$  spectral of gold and silver particles are significantly damped with no evidence of morphology-dependent resonances for  $\chi > 10$ . However, in the smaller size parameter regime, strong enhancement of the ripple structure is evident, which coincides with the condition of plasmon resonance, ie: when  $\epsilon' \approx -2\epsilon_m$ . Finally, as the optical constants of metals are wavelength dependent, the resulting spectral of  $Q_{ext}$  follow suit.

In addition, an evanescent wave results in a stronger appearances of resonances with intense peaks occurring at different size parameters for TM and TE polarizations. Also, as the incident angle approaches the critical case, penetration of an evanescent field extends deeper into the cover allowing the enhanced excitation of resonant modes in the particle. In both cases of dielectrics and metals, an enhancement of extinction efficiency was obtained for the evanescent wave with a stronger effect for TM(p-pol) polarised light, in agreement with findings in References [44] and [62].

In summary, structural resonances are influenced by the particle radius, particle index with respect to the surrounding medium, beam profile, incident angle, polarization and wavelength. Knowledge obtained will be useful in the manipulation of such particles on waveguide surfaces which is presented in later chapters. Besides, resonant structure of these particles and factors leading to the optimisation of these effects are useful especially in applications such as fluorescence and Raman sensing.